UNIVERSITÁ DEGLI STUDI DI NAPOLI FEDERICO II

FACOLTÁ DI INGEGNERIA
CORSO DI LAUREA IN INGEGNERIA AEROSPAZIALE

PROCEDURE DI CALIBRAZIONE PER UN RADAR ALTIMETRO INTERFEROMETRICO OPERANTE DA SATELLITE BASATE SU DATI DI RA-2

Relatore
Ch.mo Prof. ANTONIO MOCCIA
Correlatore
Ing. GIOVANNI ALBERTI

Candidata
MARIAFRANCESCA VALENTINO
Matr 347/584

Anno accademico 2001-2002

INTRODUCTION

Altimeter observations are recognised by the science community as integral parts of the integrated observing strategy of the World Ocean Circulation Experiment (WOCE). Availability of altimeter measurements is guaranteed in the short term over the next five years thanks to ENVISAT and JASON missions. Approximately in the same time frame, another mission CRYOSAT will provide in addition to sea surface topography also ice topography information with high resolution.

Continuity in the measurements shall however be guaranteed also in the post ENVISAT era and thus a transition towards «Operational Oceanography» is deemed necessary.

The «challenge of continuity» shall however be combined with the additional user's need for global, near real time, high accuracy and high resolution observations of sea surface topography. At present it is recognised that only altimeters can measure the sea level, but the spatial and temporal sampling capabilities of a single nadir looking altimeter system are certainly far off from the spatial and temporal sampling figures required to resolve ocean mesoscale variations and to study the effect of such fluctuations on the energetics of the mean circulation. Only multiple altimeter systems in properly combined orbits can resolve the ocean mesoscale, or alternatively some new innovative altimeter concept.

The last possibility is the main objective of the present thesis work that has been developed at CO.RI.S.TA (Consortium of Research on Advanced Remote Sensing

Systems) in the framework of IRAC study funded by ESA (European Space Agency).

IRAC stands for «Study of Innovative Radar Altimeter» and it is part of the Earth Observation Preparatory Programme (EOPP). CO.RI.S.TA is part of the working team led by Alenia Spazio with the scientific support of the Satellite Oceanography Group (SOG) of the Italian National Research Council (CNR) «Istituto di Fisica dell'Atmosfera» CNR/IFA.

The present thesis is organised as follows:

Chapter I describes the main oceanographic applications giving a scientific background and justification for the new mission.

Chapter II, after a brief survey on the possible new altimeter concepts, describes the main performance models used for designing the new system.

Chapter III describes in details the possible procedures to be used for calibrating the altimetric data from error induced by roll attitude uncertainty.

CHAPTER I

SCIENTIFIC BACKGROUND AND JUSTIFICATION

FOR NEW MISSIONS

1. Typical Oceanic Phenomena Observable by an Altimeter

Variations in sea surface height are associated both to dynamical and thermodynamical processes [1-5]. On one hand the sea elevation is related to the heat content of the whole water column, as the volume of water is modified mainly by temperature, and only to a minor extent by salt variations. On the other hand, especially at meso/large scale and in the regions away from the equator, the movement of water masses obeys, in first approximation, the geostrophic balance, which equates the pressure gradient to the coriolis force. At the surface, the pressure gradient is given by an elevation or depression of the sea level that can be detected by altimeters. Obviously, an accurate measure of the geoid is needed to obtain absolute surface geostrophic currents from altimeter data, while presently available geoid models have errors smaller than oceanographic signals only at wavelengths longer than 3000 km. As a consequence, altimeter-derived absolute ocean topography could be used to test general circulation models only at the larger scales. The ocean also responds to the gravitational attraction of the sun and moon, rising and falling each

day with amplitudes that can reach several meters. Tides are an important mechanism that has a strong impact in oceanography, and whose study took great advantage from altimetry.

Large scale ocean circulation

Our knowledge of large scale ocean circulation received major inputs from satellite altimetry [6-21]. Basing on the 8-year record of combined TOPEX/Poseidon, ERS-1 and ERS-2 data, many advances have been done in the knowledge of temporal variations of large-scale ocean processes once the tides were filtered. Large scale high-frequency barotropic variability, that was not sufficiently sampled by past in situ measurements, has been finally detected and mapped globally. Moreover, the long time series of last generation of altimeter data also allowed to better investigate at seasonal and interannual scales the characteristics of baroclinic Rossby waves. In addition, the distribution of the global annual cycle of sea level could be computed and, consequently, the steric effect was demonstrated to dominate at medium and high latitudes and the transition to the wind forcing at low latitudes resulted evident from altimeter data. Altimeter data have also caught the signal associated to the ENSO, showing that this phenomenon is not limited to the tropical Pacific, as similar changes where also observed in the Indian ocean in the same periods when stronger ENSO events were recorded. A long-term observation on global scales is clearly required to improve our understanding of the evolution and impact of these anomalies on the climate.

Mesoscale circulation

Characterizing the ocean circulation through large scale wind and thermohaline forcings is only a first order approximation of the real processes occurring in the oceans. Actually, the ocean circulation presents a somehow turbulent behaviour, which is far from being temporally stable and shows a strong variability on a wide range of spatial scales (from few tens to hundreds of kilometres). The variability is maximum at the scales of the internal Rossby radius of deformation, which is referred to as mesoscale and varies from place to place according to the local stratification and forcing. Ocean eddies, meanders, instabilities, filaments, and similar features are observed almost everywhere and their energy can exceed by an order of magnitude this of the mean flow. In this context altimeter data gave fundamental quantitative information on the eddy kinetic energy associated to the upper-ocean current system [22-31]. The correlation of EKE with the mean currents and the influence of the bathymetry has also been revealed. Moreover the variations of the eddy energy at seasonal to interannual scales could be provided for the first time on global scale. In addition to this the frequency/wavenumber spectrum of mesoscale circulation could be characterized for each area of interest.

Even if an incredible progress on our knowledge of phenomena at mesoscale was possible since the first altimeters were launched, the characteristics of the time-space sampling of existing satellite systems strongly limit the possibility to monitor mesoscale features at a high level of the accuracy that would be required also for a better assimilation into circulation models.

Tropical ocean variability

In view of the fact that most of the heat content in the tropical ocean is stored in the upper layer, low-latitude oceans are often approximated as a two layer system. Consequently, altimeter data are relatively easily applied to describe the variability of the circulation in the tropical oceans and to monitor the extreme short-term climatic events at low-latitudes, such as El Niño [32-36]. Effectively, many applications regarded the tropical Pacific because of the importance of the ENSO phenomenon, even if probably the most important contribution of altimeter data to our knowledge of tropical oceans is the possibility to describe the variability in areas that result very badly covered by in situ measurements, as in particular the Indian ocean. The data coverage of the satellite altimeters led to the identification of the existence of equatorial waves, whose propagation speed and horizontal structure could be characterized from space. The response of different seas, like the Indian ocean, the Bay of Bengal or the Arabian sea, to wind forcing could also be monitored. However, the view of the tropical ocean circulation that altimetry could offer to date is only a first limited perspective. Advances are needed for both the assimilation techniques into three-dimensional circulation models and for a higher spatial and temporal resolution of altimeter measurements.

In addition to this, it must be observed that, as sea level data are related to the subsurface thermal structure, that actually acts as a thermal memory, satellite altimeter data have a significant potential also for improving the prediction skills of coupled climate system in the tropics. This could, in turn, generate an additional operational demand for future satellite altimetry.

Ocean tides

Satellite altimetry offered for the first time a means to have an estimate of tidal oscillations over the global oceans [37-41]. Actually highly accurate tidal prediction models are required for the oceanographic exploitation of altimetric measurements from space, but, on the other hand, altimetry itself permitted an incredible improvement in the observing capabilities for tidal phenomena in the open ocean. Beside the high quality in the description of major tidal constituents, altimetry also showed that ocean response to semi-monthly and monthly forcing consists of both gravity mode and planetary-topographically trapped modes. Moreover signatures of internal tides were detected in the analysis of residual along track signals. However, one of the major limit in present tidal models is their low accuracy in shallow water areas, thus near-shore altimetric data would give a fundamental contribution also to improve the coastal areas monitoring capabilities.

Ocean surface waves and winds

One of the main practical applications for the wind and wave data derived from the altimeter measurements is the possibility to produce reliable atlas of wind and wave global conditions [42-48]. Till before the availability of these data, similar atlas were based on few sparse measurements at some fix locations and on the reports from visual observations from voluntary ships. The latter ones, which constituted more than 90% of the available information, were substantially biased towards the low values, because the ships tend naturally to avoid the stormy areas. In an extensive program for the European coasts, smart integration of model and altimeter data

provided the basic background that allowed an unprecedented accuracy in the wave data close to the coast.

On short term applications, the altimeter data, both for wind and waves, provide the essential information for the correction, by data assimilation, of the daily forecast produced by the meteorological and wave models operational at the various centres, e.g. the European Centre for Medium-Range Weather Forecasts (Reading, U.K.). These data have also allowed the identification of the problems presently encountered by global atmospheric models in the enclosed basins, specifically the Mediterranean Sea. A higher accuracy than presently available, particularly in the coastal areas, would allow a better identification of the problem, and a more likely approach to its solution.

Sea level change

Monitoring long-term sea level change is a fundamental topic for a wide variety of interests in our society. The rate at which sea level is rising as a consequence of the increasing greenhouse effect would, consequently, represent an important parameter to validate the predictions obtained from climate models. In this context, with the possibility to obtain a higher accuracy on the estimation of satellite altitude and of the corrections to be applied on the measures, altimetry revealed as a possible and important instrument to have a precise measurement of global mean sea height and of its long term variations [49-54]. A better performance of new satellites in terms of accuracy of the orbit determination and range, and the possibility of having coherent long time series would allow to estimate also the acceleration in sea level rise, which

would represent a fundamental parameter for climate monitoring and models'
validation.

2. Scientific and Practical Importance of Use of Altimeters

As soon as the first artificial satellites were launched, in the 1960s, remote sensing of
the Earth surface and in particular radar altimetry produced an incredible amount of
information on many unknown aspects of the Earth system. In facts, both
oceanography, geodesy and geophysics lived a revolutionary period as a frequent and
global measurement of the shape of the ocean and ice surface became possible.

For what concerns oceanography, in particular, it must be observed that traditional
oceanographic measurements are quite expensive and that a very long time is
necessary to cover the global oceans with these measurements, which makes a
synoptic and continuous in situ monitoring of the oceans absolutely unfeasible. As a
consequence only a 'climatologic' view of the global oceans was possible before
remote sensing systems were developed, thus missing the strong variability in ocean
circulation, salinity and temperature characteristics and their eventual interannual
changes, which obviously represent fundamental information for a better monitoring
of the oceans and for an improvement in our capability of forecasting environmental
and climatic changes.

Similarly it is not possible to monitor the growth, movement and decay of ice cover

with in situ measurements, while ice is known to play a crucial role in many physical and biological processes at high latitudes which can affect the whole Earth system. With the advent of satellite altimetry a unique tool for mapping the global topography of surface covered by the oceans and ice became available for the oceanographers community.

3. Scientific and Practical Importance of Use of Altimeters in Operational Oceanography

The importance of the operational oceanography has been recognized since the Second World Climate Conference in 1990. At that time, an international programme, the Global Ocean Observing System (GOOS) was launched, assessing the permanent global framework of observations, modelling and analysis of ocean variables needed to support operational ocean services wherever they are undertaken around the world. The European partecipation to the GOOS was promoted in 1994 with the creation of the EuroGOOS [55].

The operational oceanography consists in the systematic and long-term analysis, assimilation into numerical models and rapid dissemination of observational data concerning the state of the seas, oceans and atmosphere. Operational oceanography requires the rapid transmission of measurements to data assimilation centres, where the latest computational resources are used to generate nowcasts, forecasts and

hindcasts. This means that an accurate description of the present state of the sea can be provided in real time or in near-real time, together with a forecast of the future condition of the sea. The operational oceanography gives the possibility to assemble long term data sets that can help the description and interpretation of past states, and time series showing trends and changes.

Satellite altimetry provides continuous and quasi synoptic measurements of sea surface elevation. As a consequence, it represents one of the most promising means to describe the dynamical state of the oceans for operational purposes and has been identified of vital importance to EuroGOOS [56-58]. Satellite altimetry has been already used in the MFSPP (Mediterranean Forecasting System Pilot Project) funded by the EU-MAST Project [59] for the Mediterranean Sea, and its use is under development for the European Atlantic forecasting systems (DIADEM, FOAM, MERCATOR).

However, on one hand the nature of altimeter measurements requires innovative approaches to effectively assimilate useful information in the numerical models, on the other hand, it still results sparse in space and time compared with the ocean energy containing scales.

4. A Brief Review of the Most Important Missions for Oceanographic Studies

Since the first dedicated altimeter was launched on Seasat platform in 1978, satellite altimetry has lived an incredible and continuous development as long as new sensor were designed and became operational [60-63]. The accuracy in range measurements gradually reached values that have allowed an extraordinary increase in our knowledge of many aspects of ocean and ice dynamics and variability.

Seasat

Seasat was launched on June 28, 1978 and was the first satellite designed for remote sensing of the Earth's oceans. Its Radar Altimeter (ALT) was used to measure wave heights by measuring spacecraft altitude above the ocean surface. The experiment operated at Ku-band and had 10 cm vertical accuracy. Seasat mission was designed to demonstrate the feasibility of monitoring from space the global oceans and to help determine the requirements for an operational ocean remote sensing satellite system. The mission had the specific objectives to collect data on sea-surface winds, sea-surface temperatures, wave heights, internal waves, atmospheric water, sea ice features and ocean topography. Due to a failure of the vehicle's electric power system, the mission ended on October 10, 1978. Although only approximately 42 hours of real time data were received, the mission succeeded in demonstrating the feasibility of microwave remote sensing to monitor ocean conditions.

Geosat

Geosat was a US Navy military oceanographic satellite consisting of a radar altimeter designed to obtain closely spaced, precise mapping of the Earth's geoid over the ocean. It was designed to measure sea surface heights to within 5 cm. After a Geodetic Mission (GM) that lasted from March 1985 to September 1986, and that was originally classified by the Navy and made unavailable to the public until 1995, an Exact Repeat Mission (ERM) was initiated in November 1986 to produce more accurate sea surface profiles with a modified orbit. Since the ground tracks for the ERM were very close to the Seasat altimeter data tracks, the new data were made available to the research community, providing wind, wave and sea-level products. NASA obtained Geosat data for extensive waveform modelling and ice sheet research. Geosat supplied the scientists with the first long-term global observations of sea level, wind speed, wave height, and ice topography. Moreover, the Geosat altimeter was the only satellite to capture the sea level changes associated with the 1987 El Nino.

ERS

The first European satellite to carry a radar altimeter, ERS-1, was launched on 17 July 1991. This satellite was designed to have different orbital configurations. During the first few months, the Commissioning Phase, all instruments were calibrated and validated. Since then, ERS-1 has been flying two Ice Phases (in which the repeat period was 3 days), a Multi-Disciplinary Phase (a 35-day repeat orbit lasting from

April 1992 till December 1994), and the Geodetic Phase, which started in April 1994 and had a repeat period of 168-days. The second repeat cycle in this Phase, till the launch of ERS-2, was shifted by 8 km with respect to the first, so a ``336-day repeat'' was obtained. ERS-2 was launched on 21 April 1995 and operated simultaneously to ERS-1, until ERS-1 was retired, in March 2000. Since their launch, ERS satellites have monitored the sea surface almost continuously. The accuracy of their altimeter range measurements has been estimated to be a little under 5 cm.

TOPEX/Poseidon

TOPEX/Poseidon was launched in 1992 as joint venture between CNES and NASA. While a 3-year mission was initially planned, with a 5-year store of expendables, TOPEX/Poseidon is still flying, 9 years after its launch. Due to the low orbit inclination, data coverage is more limited respect to ERS data. However, TOPEX/Poseidon is equipped with two experimental altimeters, one French and one US-made, that reach an accuracy in sea surface height determination around 3 cm. Thanks to this high performance, for the first time, the seasonal cycle and other temporal variabilities of the ocean have been determined globally with high accuracy, yielding fundamentally important information on ocean circulation.

Envisat

In November 2001, the European Space Agency will launch Envisat, an advanced polar-orbiting Earth observation satellite which will provide measurements of the atmosphere, ocean, land, and ice over a five year period. The Envisat satellite has

been designed to ensure the continuity of the data measurements of the ESA ERS satellites. A radar altimeter (RA-2) will be mounted on Envisat. This instrument is derived from the ERS-1 and 2 Radar Altimeters, providing improved measurement performance and new capabilities determining the two-way delay of the radar echo from the Earth's surface to a very high precision, within 2.5 centimetres.

Jason-1

Jason-1 is the first follow-on to TOPEX/Poseidon mission. It will be launched in fall 2001 and will provide highly accurate ocean altimetry data and near-real time altimetry data for predicting sea state and ocean circulation. Built by CNES, Jason is a lightweight altimeter based on the experimental secondary altimeter used by TOPEX/Poseidon. A second system at microwave will be used to measure the density of water vapour in the atmosphere, which will allow much more accurate atmospheric corrections. This system is expected to measure sea surface height to within 2.5 centimetres.

CRYOSAT

CryoSat is the first satellite to be realized in the framework of the Earth Explorer Opportunity Missions of ESA's Living Planet Programme. The mission concept has been selected in 1999 with an anticipated launch in 2004. It is a radar altimetry mission dedicated to observations of the polar regions. The goal is to study possible climate variability and trends by determine variations in thickness of the Earth's continental ice sheets and marine sea ice cover. The CryoSat Mission begins with a

launch in 2004, into a near polar Low Earth Orbit (LEO) non sun-synchronous at an altitude of ~ 720 km km with an inclination of 92 degrees. The spacecraft accommodates the Altimeter SIRAL, DORIS receiver and Laser reflector.

In spite of the big progress done, still big improvements can be imagined both for what concerns an increase in the range measurements accuracy, that could allow a more precise description of sea surface topography especially for regions where dynamic signals are not particularly strong (as the Mediterranean sea), or thinking of more reliable measurements near the coasts, and finally identifying sampling strategies that could allow a more synoptic and global coverage of the Earth surface which is fundamental for a precise monitoring of mesoscale currents. It is clear, therefore, the necessity of innovative radar altimeter concepts.

The scientific team of IRAC studied the current requirements of radar altimetry for various application. The results are shown in the table in the next page.

	REQUIREMENTS						
	Spatial resolution	Along-track sampling	Cross-track sampling	Accuracy	temporal sampling	Miss Ion duration	Distance from coast
Large scale circulation/transport	50km	50km	300 km	Ongoing T/P-ERS	20 days		
Large scale propagating features (Rossby waves)	50km	50km	150 km	2 cm	15 days		
Barotropic signals			500 km	3 cm	3 days		
Open ocean mesoscale (eddies/fronts)	20km	20km	40 km	Ongoing T/P-ERS	10 days		
Semi-enclosed seas circulation	10km	10km	30 km	Ongoing T/P-ERS	10 days		
Coastal currents small-mesoscale	15 km	15 km	15 km	Ongoing T/P-ERS	5 days		15 km
Coastal tide	10 km	10 km	10 km	Ongoing T/P-ERS	not crucial		10 km
Mean sea level	NA	NA	NA	0.5 mm/y		2 decades (combined)	
Data assimilation in OGCM	Ongoing T/P-ERS	Ongoing T/P-ERS	Ongoing ERS	Ongoing T/P-ERS	10 days		10 km
Data assimilation for regional/coastal models	10 km	10 km	10 km	1-2 cm	5 days		
Wind speed	7km ~ 1s	7km ~ 1s	50km	1.5 m/s	3 days		15 km
Wave height	7km ~ 1s	7km ~ 1s	100km	0.25 m or 3% of Hs	3 days		15 km

CHAPTER II

DESIGN OF AN INNOVATIVE RADAR ALTIMETER: INTERFEROMETRIC SAR(SARIN)

1. A Brief Review Of The Investigated Measurement Techniques & System Concepts

Radar Altimeter systems designed up to now (Seasat, Geosat, ERS-1 and 2, TOPEX/POSEIDON, RA-2 Advanced Radar Altimeter for ENVISAT-1) are making use of single beam, pulse limited nadir looking configurations.

It is recognised that these systems, in spite of their proven technology and thus maturity, are limited in that they are only able to observe the single swath beneath the satellite's orbital path, prohibiting measurements of larger mesoscale phenomena like eddies and hurricanes that rapidly change with time. To view extended surfaces, these systems rely on the normal satellite orbital precession and, as a consequence, several days are required to get an entire coverage of the Earth.

A possible solution is certainly represented by a constellation of nadir looking altimeters to meet the sampling requirements of mesoscale phenomena.

This is a low technological risk solution, but it is complex and has got high costs, so it was discarded to advantage of different solutions, all based on use of a unique satellite:

- Off-Nadir

- Two Dish Interferometer Based Techniques

- SAR / SARIn Techniques

- GNSS based Techniques

- Bistatic Techniques

Off-Nadir

A first intuitive solution to the problem of spatial and temporal sampling for the ocean observations is represented by the modification of the conventional Pulse Limited radar altimeter concept by extending its limited, although high performing, nadir looking measurement capability with the inclusion of off-nadir measurements taken from additional antenna beams pointed off-nadir.

A pushbroom configuration with off-nadir beams aligned in the cross track direction can be considered. The individual beam's footprints should be spaced in the horizontal plane to achieve the swath widths needed for various scientific applications. The extent of the footprints is determined by the beam forming antenna system. The addition of off-nadir beams creates a remarkable increase in the number of intersections (crossovers) between ascending and descending tracks (Figure 1 shows the geometry of the acquisition for this kind of system).
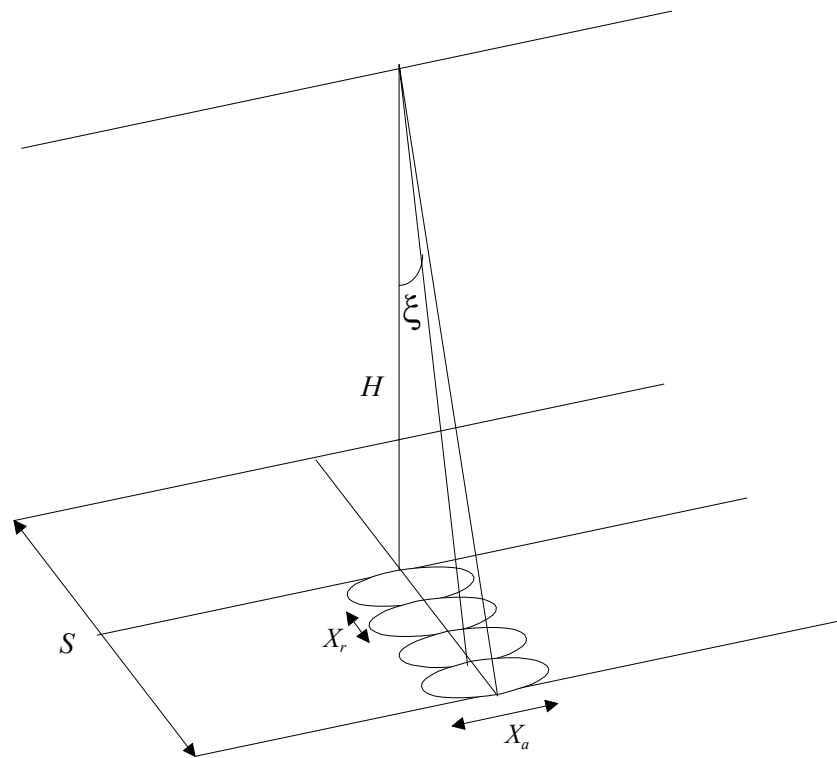
Figure 1 – Geometry of off-nadir altimetry

These crossing points have proven very important in satellite altimetry because the geoid is a constant over a given location, thus allowing its removal from the data. Assuming then that surface dynamics can be neglected or independently corrected, the crossing points can be used to identify and hence correct for orbital uncertainties and attitude uncertainties.

However, since the scattering of electromagnetic radiation by random ocean surface waves changes dramatically with the viewing incidence angle, the angle of the outermost off-nadir beams should be as small as possible to minimise the scattering variability across the swath width.

Furthermore very narrow antenna beams are dictated by the need to limit the spread in time of the return waveform which is instead caused by the fact that the transmitted pulse no more abruptly illuminates the area within the antenna footprint as in the nadir-looking geometry. To obtain a high precision range tracking a sharp backscattered waveform is needed and this is not possible for a conventional pulse limited altimeter when used in off-nadir configuration. The waveforms looses sensitivity to the sea surface roughness and broadens proportionally with the cross track swath width. Narrowing the width of the backscattered waveform, or alternatively decreasing the footprint's size reduces waveform smearing and can be achieved by using a Beam Limited rather than a Pulse Limited altimeter.

This configuration has been analysed in detail during the IRAC study and it has been recognised as a viable mean for achieving relatively accurate off-nadir altimetry. Accuracy values less than about 3 cm are possible, but the use of high frequency (Ka band) and low altitude are recommended if also good valued of spatial resolution are required (up to 5 Km).

Its accuracy is mainly limited by three factors: pulse spreading in the range direction due to the finite antenna aperture, unknown variations in the radar cross-section over the radar footprint and errors due to insufficient knowledge of the spacecraft roll angle. Unlike nadir-looking altimeters, the return waveform from a side-looking beam does not exhibit a sharp leading edge, and the accuracy with which the mean height can be tracked is governed by the accuracy with which the centroid of the return radar pulse (or a similar measure) can be determined. For side looking systems, the accuracy with which the centroid can be tracked is proportional to the radar bandwidth or number of

samples in the return, assuming Nyquist sampling, and inversely proportional to the pulse spreading, which is itself inversely proportional to the antenna dimension in the cross-track direction. The radar cross section and its angular variations are functions of wind speed and direction, and the challenge of predicting the angular and spatial variation of the cross section from the altimeter data alone with an accuracy sufficient for obtaining centimeter level height accuracy is daunting, and probably impossible to meet, given our current state of understanding.

Two Dish Interferometer Based Techniques

Another technique suited to synthesise multiple beams is based on the two element Interferometer.

This is a concept widely used in radioastronomy where interferometry is used for receiving radiation from celestial radio objects as they drift across the sky through the antenna pattern.

Figure 2 shows the involved geometry, where the two antennas are separated by a distance d in the cross track direction and have an off-nadir angle ξ.
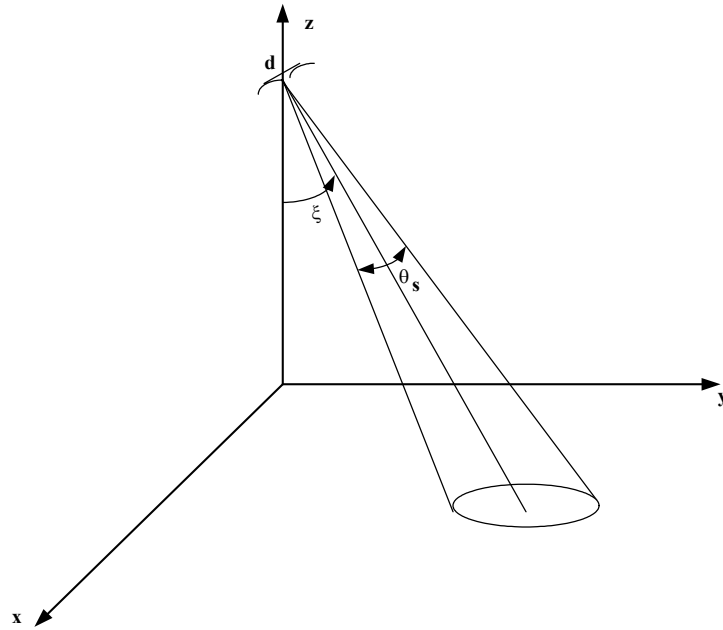
Figure 2 – Geometry of interferometric approach

In this way interference lobes are produced. The overall footprint diameter is still set by the reflectors dish diameter D while the spacing between the interference lobes is controlled by the length L of the antenna boom according to the following simple equation:

$$S = \frac{H \cdot \Delta\vartheta}{\cos^2 \vartheta} \qquad (1)$$

being:

- H the satellite altitude

- ϑ the off-nadir angle

- $\Delta\vartheta$ the angular separation of the interference lobes given by:

$$\Delta\vartheta = \frac{\lambda}{L \cdot \cos\vartheta} \qquad\qquad (2)$$

- L is the antennas separation

In our application it is then sufficient to properly track the echo within the main interference lobe of the produced interference pattern whose location on ground matches with the one established by the off-nadir looking angle.

Also in this kind of system, a trade-off between the widely used Ku – 13.5 Ghz frequency and the Ka – 36 Ghz frequency is a key issue.

The major criticality in such a system is represented by the boom length and its mechanical stability, which, combined with the attitude errors of the platform, puts severe limitations in the system performance achievable. The separation L between the two antenna dishes is in fact strictly related to the angular separation of the interference lobes, as already outlined, and thus to the spatial resolution.

The interferometric approach allows to narrow the resulting pattern aperture and to increase the number of measurements per orbit. But this method shows different drawback:

1. the improvement of the composite antenna pattern is limited only to one or two beams;

2. too many lobes are very similar in appearance. From a measurement standpoint, it would be impossible to tell a priori which lobe represents the return from the desired cell position on the earth. Therefore designing a tracker would be very

risky because of the possibility that it would jump to the adjacent late or early lobes;

3. the system is too much dependent on the knowledge of pointing angle and direction.

SAR / SARIn Techniques

SAR/SARIn techniques once combined with standard nadir looking altimetry can provide the basic means for the solution of two classes of problems:

- Need to improve the spatial resolution in order to better observe sloped surfaces and thus variable topographies.

- Need for simultaneous accessibility of wide ocean regions thus meeting temporal and spatial sampling requirements at the same time with possibly one satellite only.

Basically, this technique is a near-nadir SAR interferometric system that is able to achieve high accuracy measurements with low resolution (WSOA, Wide Swath Altimeter). By using two pairs of antennas looking left and rightward it is also possible to double the instrument coverage.

It is not afflicted by the problems we have seen in the off-nadir technique since the topography retrieval is based on the phase and, thus, the measurements become independent of the signal amplitude.

A possible observation geometry and concept operation is depicted in Figure 3.

Through the rectangular antenna pairs two swaths, 100 km each, aside of the sub-satellite track can be synthesised.

As it is obvious from general interferometry theory [64] [65], from the phase difference between the signals collected from two antennas looking at the same scene the surface height and cross track position within the swath of each pixel can be derived once the observation geometry is known.
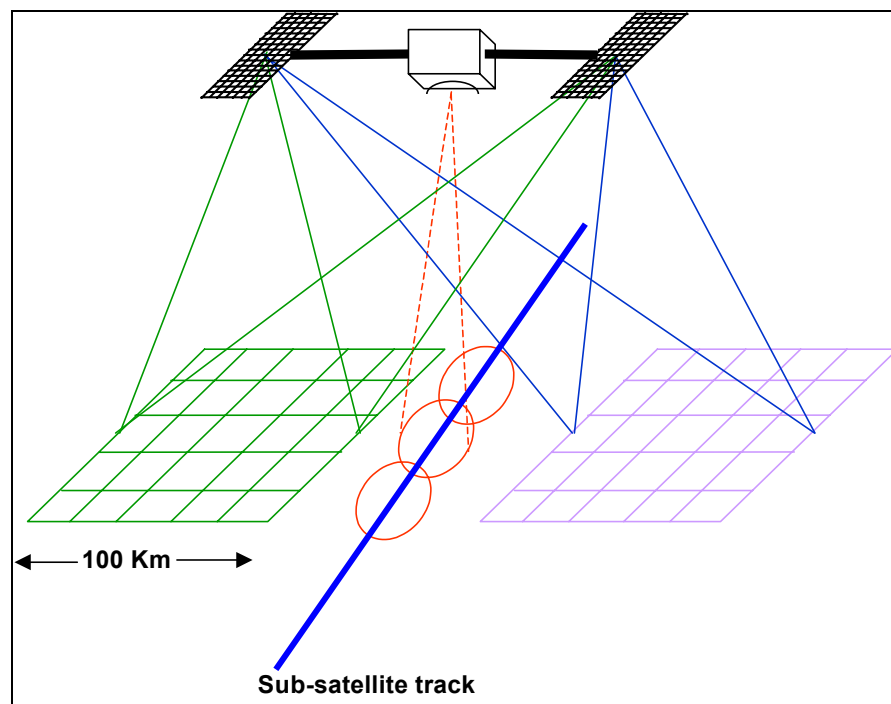
Figure 3 – Possible geometry of near-nadir interferometry

The major difference with respect to Synthetic Aperture Radar Interferometry is that the resolution required for the ocean applications is much less stringent than that requested to conventional SARIn applications. As a matter of fact 10x10 km resolution are proposed for this measurement concept stated that global characterisation of ocean mesoscale eddies requires global coverage every 10 days minimum, with centimetric height accuracy (less than 3 cm). The coarse spatial resolution allows to simplify the complexity of the system so that simple on board processing can be used.

Of course, there are intrinsic elements in the measurement concept like the control of the roll angle which are extremely critical if centrimetric accuracies are desired as in the ocean topography retrieval case. As pure indication a roll angle error of 0.1 arcsec produces an error of 5 cm in the height retrieval process. Roll angle can be compensated using different calibration procedures that are the main objectives of this thesis work.

Other important error sources are represented by the baseline stability. A variation in its length comparable to the radar wavelength will determine phase errors which may prevent correct operation of the system. In essence the thermoelastic properties of the boom have to be carefully studied to mitigate the problem.

Bistatic Techniques

It is fundamentally based on bistatic operation at points off-nadir between pairs of spaceborne altimeters. This possibility would halve the number of satellites originally required in a constellation of nadir-looking altimeters.

A main advantage is that very narrow antenna beams as in off-nadir monostatic altimetry are no more required. Demand for narrow beams (much less than 1 degree) in off-nadir altimetry was driven by the need to limit the spread of the echo leading edge over time.

In a straightforward way, a bistatic radar system is defined when antennas for reception and transmission are physically separated. In this case, the location of the target (T) depends on the distance between the transmitting and receiving antennas (S1 and S2), called baseline, and the measured propagation path. The targets for which the sum of distances from the transmitting and receiving antennas is constant, can not be resolved in distance by the bistatic system. These point targets identify in the three-dimensional space an ellipsoid and its intersection with a generic plane determines ellipsoidal isorange contours.

By considering a pair of satellite radar altimeters at an altitude h,

Figure 4 shows the isorange contours on a plane Γ tangent to the Earth surface. The tangent point for which the sum of the distances from the two satellites is minimal is called bistatic point and it is characterised by a bistatic angle θ from the S1 nadir direction.
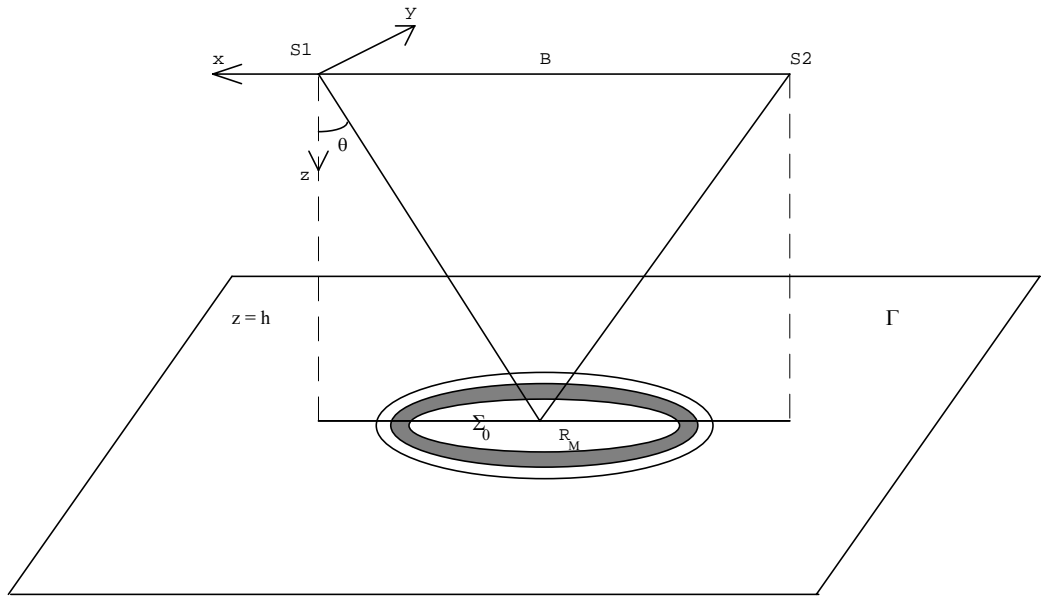
Figure 4 - Simplified Bistatic Geometry

In the monostatic case, the isorange contours are circles and the area delimited by two consecutive ones is constant over the swath and it is given by:

$$\Delta S_{mo} = \pi rh$$

(3)

where r is the radar resolution.

The last property is also satisfied in the bistatic configuration, where the area delimited by two consecutive ellipses can be written as:

$$\Delta S_{bi} \approx \frac{\pi hr}{\cos^2 \theta}$$

(4)

The fact that the isorange lines are assimilated to ellipses over the observed surfaces, leads to an echo model which, at a first glance, has some similarities with the well-known Brown model of the monostatic nadir-looking geometry. This is a main advantage respect to off-nadir altimetry: the off-nadir observation geometry causes, in fact, broadening of the echo leading edge which, in turn, reflects in reduced sensitivity to sea surface roughness and worsening of topography estimation algorithms performance. An analytical derivation of the echo model applicable in the bistatic geometry is available in the TOS report [66].

As far as the bistatic cross-section, which impacts on the resulting Signal to noise Ratio and thus contributes to dictate the performance of the measurement concept, the small bistatic angles involved in the altimetry case as well as the gently undulating surfaces of large radius of curvature compared with the incidence wavelength in the Kirchhoff approximation, entail a very slight variation from the value used in the monostatic case. Therefore, switching from monostatic to bistatic configuration, the changes in the expected SNR can be mainly associated with the different antenna pattern weight and the variation of the corresponding scattering area.

Various satellite constellations can be considered with different orbit solutions, either based on Sun Synchronous options or not to figure out the bistatic implementation approach.

1.1. Conclusion

A set of possible system solutions has been identified. The optimal solutions lead to the definition of altimetry systems which are compliant with the most part of user requirements, whereas the so called «sub-optimal solutions» correspond to systems at a lower cost which meet only a sub-set of the specified requirements.

Since the beginning of this study the «IRAC Scientific Team» has stressed the concept that the innovative altimeter should have been capable of observing mesoscale ocean phenomena. Therefore, starting from the «IRAC proposal», particular attention has been paid to altimetry techniques which allow to increase the number of mesaurements.

Optimal solutions would be constellation of satellites, specially that composed by WSOAs. Nevertheless , as we have said in a previous section, ESA has directed its attention on low cost innovative radar altimeter concepts, consequently, considering only sub-optimal solution, after a deep analysis based on a direct comparison between user requirements and achievable performances, the Wide Swath Altimeter (known as Near Nadir SAR Interferometry, too) has been recognised as the most interesting candidate for the role of innovative altimeter. Its preliminary design is outlined in next paragraphs.

2. The Near Interferometry Altimetry (WSOA)

2.1. SAR Basic Concepts

Satellite radar altimetry is well established over oceans. The implemented systems have reached a level of sophistication that are able to measure ocean topography along the nadir track with an accuracy of few centimeters.

However, land and ice topography mapping, due to high spatial variations and large local slopes, requires further improvements in order to reduce the spatial resolution.

This means to give up to the traditional pulse limited systems and to address efforts in designing suitable beam limited radar altimeters.

The latter constitutes an attractive challenge because very narrow beams are required which imply the use of large antennas and high operative frequencies.

In fact, the −3dB antenna apertures along x and y axes (ϑ_{3x} and ϑ_{3y}) are function of the used wavelength and physical antenna area A through the following:

$$\vartheta_{3x}\vartheta_{3y} = \eta_t^2 \frac{\lambda^2}{A} \tag{5}$$

where η_t is a factor depending on the used illumination tapering which at least is equal to 0.88 for an uniform illumination.

Therefore, the area A_i intersected on the surface by the −3dB antenna beam from an

altitude h, i.e. the area of the beam limited footprint, can be written as:

$$A_b \approx \eta_t^2 \frac{\pi\lambda^2 h^2}{4A}$$ (6)

The technique for synthesising large antenna through radar motion is well established for side-looking systems able to produce high resolution images [67]. In these systems the along track resolution is significantly improved by exploiting the Doppler shift caused by the relative motion between the radar and the imaged surface.

The final effect can be viewed as a remarkable reduction of the antenna aperture in the direction of motion (along track).

This basic principle is certainly applicable to radar altimeters, taking into account the differences between instruments, mainly in terms of required resolution and application.

The Doppler effect is a frequency shift measured in the received signal due to the distance variation between source and target.

If an ideal transmitted impulse is transmitted, the received signal will be shifted in frequency by an amount proportional to the variation of the radar-target distance, given by:

$$f_d = -\frac{2}{\lambda}\frac{d}{dt}R(t)$$ (7)

With respect to Figure 5, we have:

$$R(t) = \overline{SP} = \sqrt{x^2(t) + y_0^2 + (h - z_0)^2} \tag{8}$$

$$\frac{d}{dt} R(t) = \frac{v^2 t}{R(t)} \tag{9}$$

supposing that the radar is moving along a straight trajectory with constant altitude and velocity ($x(t) = vt$). Consequently:

$$f_d(t) = -\frac{2}{\lambda} \frac{v^2 t}{R(t)} \tag{10}$$
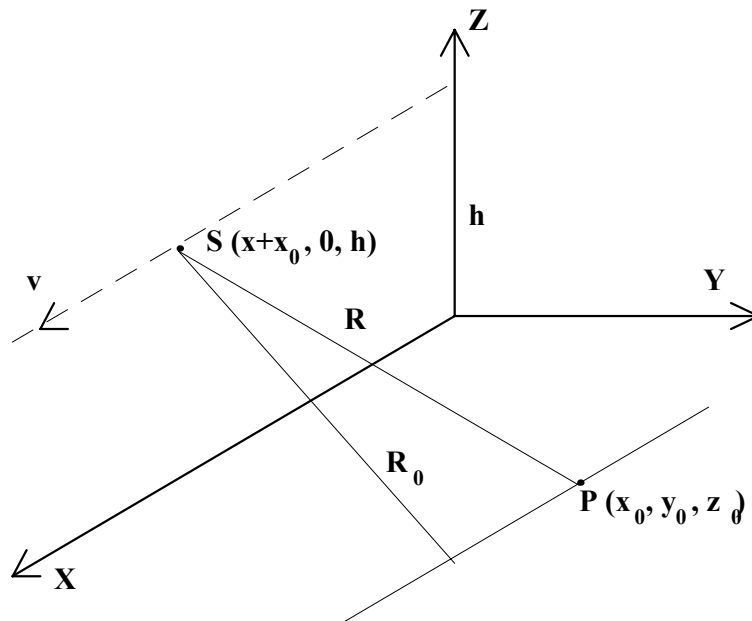
Figure 5 – Reference geometry for synthetic aperture altimetry.

Therefore, the signal coming from a single point target presents a time varying frequency, i.e. it covers a frequency band whose width depends on the time interval T within which the target is observed. Greater the so called integration time T will be, wider the signal band will result.

Naturally, the upper limit for the values of T is imposed by the received signal power which, through the attenuation introduced by the antenna pattern, determines the useful frequency band and, consequently, the spatial resolution attainable by the system.

Conventionally, the –3dB band is used (B), for which the corresponding resolution r is given by:

$$r = \frac{v}{B} \tag{11}$$

Neglecting the relative range variations, the signal power decrease is mainly due to antenna pattern. Consequently, the received band B will correspond to an integration time determined by the –3dB antenna aperture ϑ_3 and given by:

$$T_i \approx \frac{\vartheta_3 R_0}{v} \tag{12}$$

being R_0 the minimum radar-target distance where is conventionally posed the time origin, i.e.

$$R_0 = R(0) = \sqrt{y_0^2 + (h - z_0)^2} \tag{13}$$

Therefore the signal frequency band and the corresponding spatial resolution are given by:

$$\begin{cases} B = \left| f_d\left(\frac{T}{2}\right) - f_d\left(-\frac{T}{2}\right) \right| = \frac{2v^2 T_i}{\lambda R\left(\frac{T_i}{2}\right)} = \frac{2v^2 T_i}{\lambda R_0} \frac{1}{\sqrt{1 + \frac{v^2 T_i^2}{4R_0^2}}} \\ r = \frac{\lambda R_0}{2vT_i} \sqrt{1 + \frac{v^2 T_i^2}{4R_0^2}} \end{cases} \tag{14}$$

Being:

$$\frac{vT_i}{2R_0} << 1 \tag{15}$$

The latter expression can be approximated as:

$$r \approx \frac{\lambda R_0}{2vT_i} = \frac{\lambda}{2\vartheta_3} \tag{16}$$

which is the well known theoretical resolution for synthetic aperture radar system. In this case, on the contrary of real aperture radar systems, the resolution is independent on radar-surface distance.

In other words, by exploiting the frequency band caused by the Doppler effect, the system is able to «synthesise» a very large antenna in the sense that it is able to attain a spatial resolution which would have been reached by a conventional radar with a very narrow beam ϑ_{sth} given by:

$$\vartheta_{sth} = \frac{r}{R_0} \approx \frac{\lambda}{2vT_i} \approx \frac{\lambda}{2\vartheta_3 R_0} \qquad (17)$$

In this way, resolutions of few meters can be reached, but quite sophisticated data processing is required.

The phase variation introduced by the Doppler should be compensated through adequate complex filters which, in addition, are intrinsically bidimensional.

Instead, a synthetic aperture radar altimeter should perform data processing in real time on board and, moreover, resolutions such those attainable with accurate bidimensional processing are absolutely not needed. The integration time can be reduced until values for which the required data processing results significantly simplified. In particular, an integration time can be defined for which none phase compensation is required.

In fact, it can be shown that, if the phase variation along a synthetic aperture is not exceeding about , a processing without phase compensation introduces negligible errors. In this case the processing is called unfocused.

Being the phase variation along a synthetic aperture given by:

$$\varphi(t) = \frac{4\pi}{\lambda} R(t) \qquad (18)$$

the unfocused condition is equivalent to:

$$\varphi(t) - \varphi(0) \leq \frac{\pi}{4} \Longrightarrow \sqrt{x^2(t) + y_0^2 + (h - z_0)^2} - R_0 \leq \frac{\lambda}{16} \qquad (19)$$

which, after some approximations, enables to define the unfocused integration time T_u as:

$$T_u = \frac{2}{v} \sqrt{\frac{\lambda h}{8}} \qquad (20)$$

Following the (13), the equivalent –3dB antenna aperture and the spatial resolution corresponding to this integration time are:

$$\vartheta_u = \sqrt{\frac{\lambda}{2h}} \qquad\qquad r_u = \sqrt{\frac{h\lambda}{2}} \qquad (21)$$

These parameters correspond to the equivalent along-track antenna aperture and spatial resolution and they are plotted in Figure 6 for an operating frequency of 13.5 GHz. An unfocused processing is equivalent to process only a small fraction of the available Doppler bandwidth, enabling, therefore, to perform large number of multilook. It is worth noting that in this case the resolution is dependent on the spacecraft altitude.
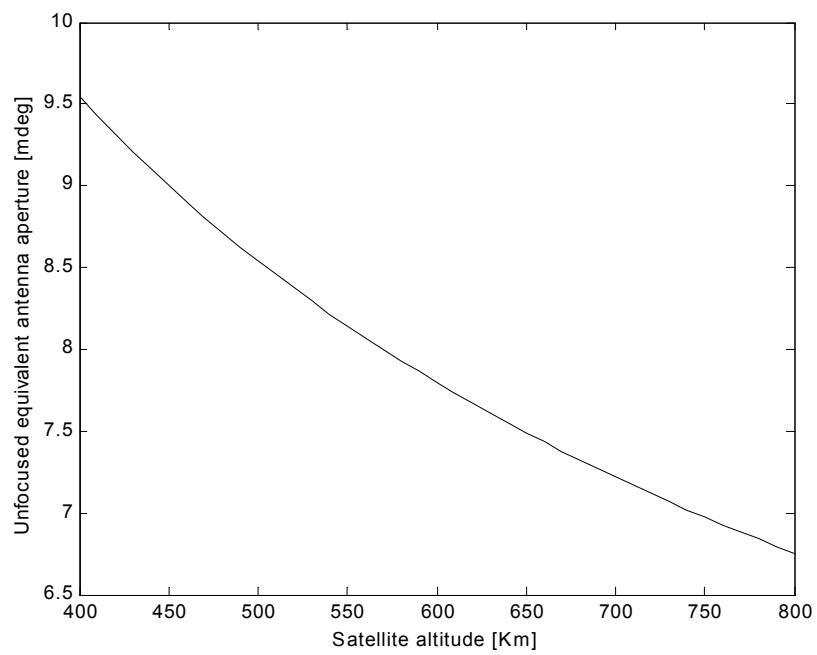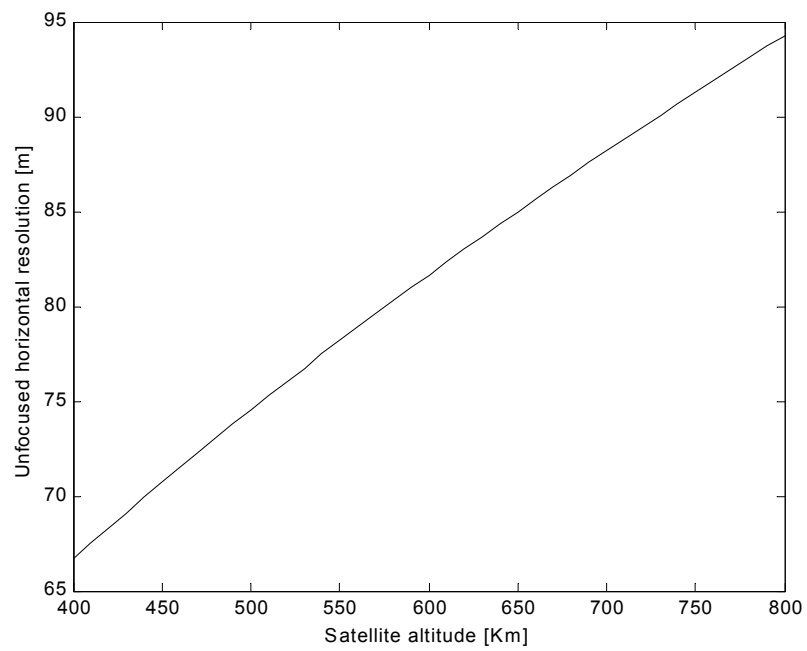
Figure 6– Unfocused resolution and equivalent antenna aperture as a function of satellite altitude for an operating frequency of 13.5 GHz

2.2. SARIn accuracy concepts

In this paragraph it is examined the estimation of topographic height from the differential range measured by two radar antennas looking at the same surface.

In Figure 7 is represented a basic imaging geometry for SARIn systems, where S1 and S2 represents two antennas viewing the same surface simultaneously and separated by a baseline vector $\underline{B}$ with length B.

The origin of the reference frame is the antenna S1 of the interferometric system. The positive z-axis points toward the Earth's centre and x-axis in direction of the satellite velocity vector. The y-axis is chosen so as to form a right-handed set of coordinate axes. From the Figure 8 we obtain:

$$R_1 = (H + r_e) \cdot \cos(\theta) - \sqrt{(h + r_e)^2 - [(H + r_e) \cdot \text{sen}(\theta)]^2} \tag{22}$$

where r_e is the Earth's radius, H is the altitude of the system respect to the Earth's surface and θ is the angle from the z-axes to $\underline{R}_1$. After some algebra the last expression can be written as:

$$R_1 = \cos(\theta) \cdot \left[H + r_e \cdot \left(1 - \sqrt{1 + \frac{2 \cdot [h - H \cdot (1 - \cos^2(\theta))]}{r_e \cdot \cos^2(\theta)} + \frac{h^2 - H^2 \cdot (1 - \cos^2(\theta))}{r_e^2 \cdot \cos^2(\theta)}} \right) \right]$$

$$\tag{23}$$

From the previous equation, considering flat surface, it is possible to neglect the third

term in the square root, and considering the approximation:

$$x \to 0 \quad \Rightarrow 1 - \sqrt{1+x} \approx -\frac{1}{2}x \tag{24}$$

we obtain: $\qquad\qquad R_1 = \dfrac{H-h}{\cos(\theta)}$ (25)

that is the very famous relation that alloy h to R_1 in the flat surface case. The

expression of h can be obtained from (22):

$$h = \sqrt{\left[(H + r_e) \cdot \cos(\theta) - R_1\right]^2 + \left[(H + r_e) \cdot \mathrm{sen}(\theta)\right]^2} - r_e \tag{26}$$
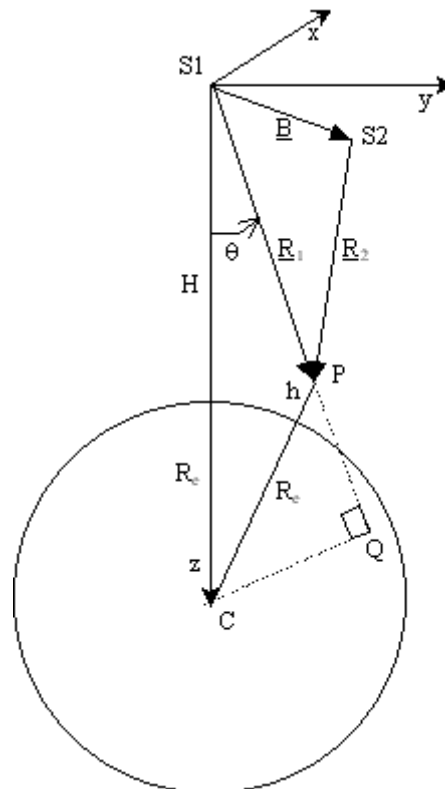
Figure 7 – Imaging Geometry for SAR Interferometry

If we define Φ the phase differences of the two antennas it is possible to write:

$$\Phi = k(R_1 - R_2) = k\left(R_1 - \sqrt{B^2 + R_1^2 - 2 \cdot \langle \underline{R}_1 ; \underline{B} \rangle}\right)$$

(27)

where the symbol $\langle \rangle$ indicate the scalar product and B is the baseline length.
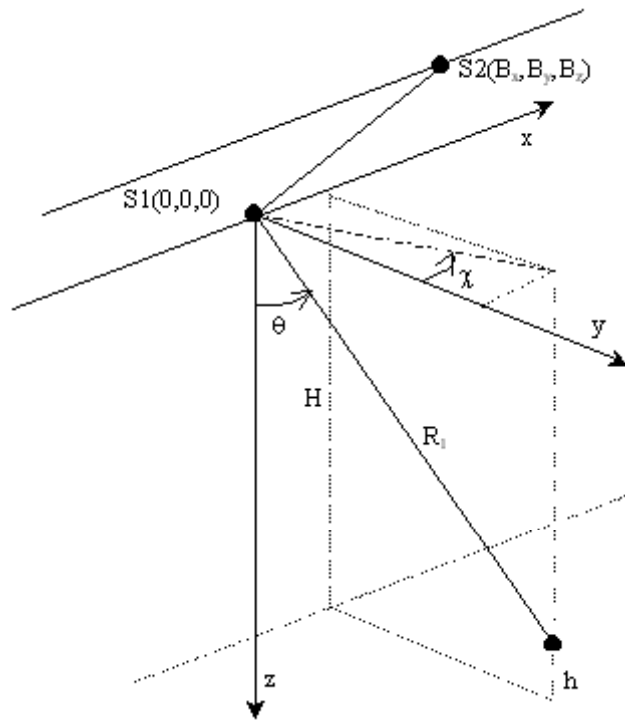
Figure 8 – Reference frame: angle χ

After some algebra we obtain:

$$\Phi = k\left(R_1 - \sqrt{B^2 + R_1^2 - 2 \cdot R_1 \left[B_x \, sen(\theta)sen(\chi) + B_y \, sen(\theta)cos(\chi) + B_z \, cos(\theta) \right]} \right)$$

(28)

Where χ is the angle from the y-axes and the projection on the x-y plane of the vector R_1, and B_x, B_y e B_z are the three components of the baseline.

Since the two antennas are fixed to the aircraft, an attitude manoeuvre involves a spin of the baseline that can be expressed in terms of the angles of (α), pitch (β) and yaw (γ). The transformation matrix to pass to the new baseline components are:

$$E = \begin{pmatrix} \cos\beta \cdot \cos\gamma & \cos\beta \cdot sen\,\gamma & -sen\,\beta \\ -\cos\alpha \cdot sen\,\gamma + sen\,\alpha \cdot sen\,\beta \cdot \cos\gamma & \cos\alpha \cdot \cos\gamma + sen\,\alpha \cdot sen\,\beta \cdot sen\,\gamma & sen\,\alpha \cdot \cos\beta \\ sen\,\alpha \cdot sen\,\gamma + \cos\alpha \cdot sen\,\beta \cdot \cos\gamma & -sen\,\alpha \cdot \cos\gamma + \cos\alpha \cdot sen\,\beta \cdot sen\,\gamma & \cos\alpha \cdot \cos\beta \end{pmatrix}$$

(29)

The expressions (26) and (28) with the transformation matrix (29) can be utilized to express h in terms of all the parameters of the system.

2.3. Topography Height Accuracy

By considering the expression (26), (28) and (29), it is interesting to note that the height is dependent from H, R_1, r_e, θ, B_x, B_y B_z χ α, β and γ. Moreover, it is supposed that the uncertainties with which are known the parameters that appear in (26), (28) and (29) are independent; in such way we can write the uncertainty of the height as the sum of the uncertainties (variances) of the single parameters.

If we indicate with $\sigma^2{}_h$ the height uncertainty obtain:

$$\sigma_h^2 = \left(\frac{\partial h}{\partial H}\right)^2 \sigma_H^2 + \left(\frac{\partial h}{\partial R_1}\right)^2 \sigma_{R_1}^2 + \left(\frac{\partial h}{\partial \Phi}\right)^2 \sigma_\Phi^2 + \left(\frac{\partial h}{\partial B_x}\right)^2 \sigma_{B_x}^2 + \left(\frac{\partial h}{\partial B_y}\right)^2 \sigma_{B_y}^2 + \left(\frac{\partial h}{\partial B_z}\right)^2 \sigma_{B_z}^2 +$$

$$+ \left(\frac{\partial h}{\partial \chi}\right)^2 \sigma_\chi^2 + \left(\frac{\partial h}{\partial \alpha}\right)^2 \sigma_\alpha^2 + \left(\frac{\partial h}{\partial \beta}\right)^2 \sigma_\beta^2 + \left(\frac{\partial h}{\partial \gamma}\right)^2 \sigma_\gamma^2$$

$$(30)$$

It is important to notice that, based on the assumption of fixed antennas to the platform, such derivatives can be calculated considering null the attitude angles (but not their uncertainties!) and therefore to derive (26) around the point:

$B_x = B_x$
$B_y = B_y$
$B_z = B_z$
$\theta = \theta$
$R_1 = R_1$ (31)
$H = H$
$\alpha = 0$
$\beta = 0$
$\gamma = 0$

The next expressions represent the first derivative of Φ function with respect previous parameters:

$$\frac{\partial \Phi}{\partial \theta} = k \frac{R_1}{R_2} \Big(B_x \cos(\theta)\operatorname{sen}(\chi) + B_y \cos(\theta)\cos(\chi) - B_z \cdot \operatorname{sen}(\theta) \Big) \tag{32}$$

$$\frac{\partial \Phi}{\partial B_x} = -k \frac{B_x - R_1 \operatorname{sen}(\theta)\operatorname{sen}(\chi)}{R_2} \tag{33}$$

$$\frac{\partial \Phi}{\partial B_Y} = -k \frac{B_y - R_1 \operatorname{sen}(\theta)\cos(\chi)}{R_2} \tag{34}$$

$$\frac{\partial \Phi}{\partial B_z} = -k \frac{B_z - R_1 \cdot \cos(\theta)}{R_2} \tag{35}$$

$$\frac{\partial \Phi}{\partial \alpha} = k \frac{R_1}{R_2} \Big[B_x \operatorname{sen}(\theta)\operatorname{sen}(\chi) - B_y \cos(\theta) + B_z \operatorname{sen}(\theta)\cos(\chi) \Big] \tag{36}$$

$$\frac{\partial \Phi}{\partial \beta} = k \frac{R_1}{R_2} \Big[B_x \cos(\theta) + B_y \operatorname{sen}(\theta)\cos(\chi) - B_z \operatorname{sen}(\theta)\operatorname{sen}(\chi) \Big] \tag{37}$$

$$\frac{\partial \Phi}{\partial \gamma} = k \frac{R_1}{R_2} \Big[-B_x \operatorname{sen}(\theta)\cos(\chi) + B_y \operatorname{sen}(\theta)\operatorname{sen}(\chi) + B_z \cos(\theta) \Big] \tag{38}$$

$$\frac{\partial \Phi}{\partial \chi} = k \frac{R_1}{R_2} \Big[B_x \operatorname{sen}(\theta)\cos(\chi) - B_y \operatorname{sen}(\theta)\operatorname{sen}(\chi) \Big] \tag{39}$$

Moreover:

$$\frac{\partial h}{\partial \theta} = \frac{R_1 \cdot (H + r_e) \cdot \operatorname{sen}(\theta)}{h + r_e} \tag{40}$$

After some algebra obtain the first derivative that are present in (30).

$$\frac{\partial h}{\partial H} = \frac{H + r_e - R_1 \cdot \cos(\theta)}{h + r_e}$$

(41))

$$\frac{\partial h}{\partial R_1} = \frac{R_1 - (H + r_e) \cdot \cos(\theta)}{h + r_e}$$

(42)

$$\frac{\partial h}{\partial \Phi} = \frac{\partial h}{\partial \theta} \cdot \frac{1}{\frac{\partial \Phi}{\partial \theta}} = \frac{(H + r_e) \operatorname{sen}(\theta)}{h + r_e} \cdot \frac{R_2}{k(B_x \cos(\theta) \operatorname{sen}(\chi) + B_y \cos(\theta) \cos(\chi) - B_z \cdot \operatorname{sen}(\theta))}$$

(43)

$$\frac{\partial h}{\partial B_x} = \frac{\partial h}{\partial \theta} \cdot \frac{1}{\frac{\partial \Phi}{\partial \theta}} \cdot \frac{\partial \Phi}{\partial B_x} = -\frac{(H + r_e) \cdot \operatorname{sen}(\theta)}{h + r_e} \cdot \frac{B_x - R_1 \operatorname{sen}(\theta) \operatorname{sen}(\chi)}{B_x \cos(\theta) \operatorname{sen}(\chi) + B_y \cos(\theta) \cos(\chi) - B_z \cdot \operatorname{sen}(\theta)}$$

(44)

$$\frac{\partial h}{\partial B_y} = \frac{\partial h}{\partial \theta} \cdot \frac{1}{\frac{\partial \Phi}{\partial \theta}} \cdot \frac{\partial \Phi}{\partial B_y} = -\frac{(H + r_e) \cdot \operatorname{sen}(\theta)}{h + r_e} \cdot \frac{B_y - R_1 \operatorname{sen}(\theta) \cos(\chi)}{B_x \cos(\theta) \operatorname{sen}(\chi) + B_y \cos(\theta) \cos(\chi) - B_z \cdot \operatorname{sen}(\theta)}$$

(45)

$$\frac{\partial h}{\partial B_z} = \frac{\partial h}{\partial \theta} \cdot \frac{1}{\frac{\partial \Phi}{\partial \theta}} \cdot \frac{\partial \Phi}{\partial B_z} == -\frac{(H + r_e) \cdot \operatorname{sen}(\theta)}{h + r_e} \cdot \frac{B_z - R_1 \cdot \cos(\theta)}{B_x \cos(\theta) \operatorname{sen}(\chi) + B_y \cos(\theta) \cos(\chi) - B_z \cdot \operatorname{sen}(\theta)}$$

(46)

$$\frac{\partial h}{\partial \alpha} = \frac{\partial h}{\partial \theta} \cdot \frac{1}{\frac{\partial \Phi}{\partial \theta}} \cdot \frac{\partial \Phi}{\partial \alpha} = \frac{R_1 \cdot (H + r_e) \cdot \operatorname{sen}(\theta)}{h + r_e} \cdot \frac{B_x \operatorname{sen}(\theta) \operatorname{sen}(\chi) - B_y \cos(\theta) + B_z \operatorname{sen}(\theta) \cos(\chi)}{B_x \cos(\theta) \operatorname{sen}(\chi) + B_y \cos(\theta) \cos(\chi) - B_z \cdot \operatorname{sen}(\theta)}$$

(47)

$$\frac{\partial h}{\partial \beta} = \frac{\partial h}{\partial \theta} \cdot \frac{1}{\frac{\partial \Phi}{\partial \theta}} \cdot \frac{\partial \Phi}{\partial \beta} = \frac{R_1 \cdot (H + r_e) \cdot \operatorname{sen}(\theta)}{h + r_e} \cdot \frac{B_x \cos(\theta) + B_y \operatorname{sen}(\theta) \cos(\chi) - B_z \operatorname{sen}(\theta) \operatorname{sen}(\chi)}{B_x \cos(\theta) \operatorname{sen}(\chi) + B_y \cos(\theta) \cos(\chi) - B_z \cdot \operatorname{sen}(\theta)}$$

(48)

$$\frac{\partial h}{\partial \gamma} = \frac{\partial h}{\partial \theta} \cdot \frac{1}{\frac{\partial \Phi}{\partial \theta}} \cdot \frac{\partial \Phi}{\partial \gamma} = \frac{R_1 \cdot (H + r_e) \cdot \operatorname{sen}(\theta)}{h + r_e} \cdot \frac{-B_x \operatorname{sen}(\theta) \cos(\chi) + B_y \operatorname{sen}(\theta) \operatorname{sen}(\chi) + B_z \cos(\theta)}{B_x \cos(\theta) \operatorname{sen}(\chi) + B_y \cos(\theta) \cos(\chi) - B_z \cdot \operatorname{sen}(\theta)}$$

(49)

$$\frac{\partial h}{\partial \chi} = \frac{\partial h}{\partial \theta} \cdot \frac{1}{\frac{\partial \Phi}{\partial \theta}} \cdot \frac{\partial \Phi}{\partial \chi} = \frac{R_1 \cdot (H + r_e) \cdot sen(\theta)}{h + r_e} \cdot \frac{B_x \ sen(\theta)\cos(\chi) - B_y \ sen(\theta)sen(\chi)}{B_x \ \cos(\theta)sen(\chi) + B_y \ \cos(\theta)\cos(\chi) - B_z \cdot sen(\theta)}$$

$$(50)$$

Finally, the phase uncertainty σ_Φ^2 can be obtained from the Cramer-Rao bound:

$$\sigma_\Phi^2 = \frac{1}{2N_L} \frac{1 - \gamma^2}{\gamma^2} \qquad (51)$$

where N_L is the number of looks that are considered. γ is the correlation coefficient between two interferometric images that is obtained from:

$$\gamma = \frac{|\alpha|}{1 + SNR^{-1}} \qquad (52)$$

$$|\alpha| = \left(1 - \frac{|B_x|\rho_x}{R\lambda}\right)\left(1 - \frac{|B_y|\rho_{gr}}{R\lambda}\right) sinc\left[\frac{\delta_x}{\rho_x}\left(1 - \frac{|B_x|\rho_x}{R\lambda}\right)\right] sinc\left[\frac{\delta_r}{\rho_r}\left(1 - \frac{|B_y|\rho_{gr}}{R\lambda}\right)\right]$$

$$(53)$$

where (ρ_x, ρ_{gr}) are the azimuth and ground range resolutions and (δ_x, δ_{gr}) are the mis-registration errors. The signal to noise ratio is evaluated in the next paragraph.

2.4. Signal to noise ratio

In the case of SARInt configuration, the well known following expression can be used:

$$SNR = \frac{P_p G^2 \lambda^2}{(4\pi)^3 R^4} \sigma \frac{1}{KT_0 F B_n} \frac{1}{L_a L_{RF}} \tag{54}$$

where:

P_p is the transmitted peak power;
G is the antenna pattern gain;
R is the distance between radar and target;
λ is the wavelength;
σ is the equivalent target's radar cross section;
$kT_0 B_n F$ is the noise power, being k the Boltzman constant, F the receiver noise figure, T_0 the system noise temperature and B_n the equivalent noise bandwidth;
N is the noise power;
L_a Are the total atmospheric losses.
L_{RF} Are the radio-frequency losses.

As far as synthetic aperture processing is considered, the target is represented by a resolution cell and the improvement given by the number of pulses integrated N_p should be added. The last expression becomes:

$$SNR = \frac{P_p \tau N_p G^2 \lambda^2}{(4\pi)^3 R^4} \overline{\sigma^0} \frac{\rho_R \rho_x}{\sin \vartheta} \frac{1}{KT_0 F} \frac{1}{L_a L_{RF}} \tag{55}$$

where θ is the off-nadir angle of the considered cell and τ is the transmitted pulse length. Our aim is to guarantee a good signal to noise ratio for each cell in order to retrieve an height information with a good degree of accuracy over all the image. The variation of the signal to noise ratio depends only on the variation of the off-nadir angle along the swath. Assuming a Gaussian law for the antenna pattern, such as:

$$G(\vartheta) = G_{max} \; \exp\left[-\log 2 \frac{\sin^2(\vartheta - \vartheta_0)}{\sin^2(\vartheta_3/2)}\right] \tag{56}$$

where ϑ_3 is the -3 dB antenna aperture in the elevation and ϑ_0 is the antenna pointing angle. Considering the following expression for the maximum gain of the antenna pattern:

$$G_{max} = \frac{4\pi}{\lambda^2} \eta_{tot} A \tag{57}$$

where η_{tot} is the total antenna efficiency and A is its physical area, the signal to noise ratio can be rewritten as:

$$SNR = \frac{P_p \tau \rho_R \rho_x N_p (\eta_{tot} A)^2}{4\pi\lambda^2 R^4} \, \overline{\sigma^0} \, \frac{1}{KT_0 F} \, \frac{1}{L_a L_{RF}} \, \frac{\exp\left[-2\log 2 \frac{\sin^2(\vartheta - \vartheta_0)}{\sin^2(\vartheta_3/2)}\right]}{\sin\vartheta} \tag{58}$$

Form the last expression it is evident that the minimum value of the signal to noise ratio occurs at the and of the swath, i.e. in correspondence with the maximum off-nadir angle.

2.5. Near-nadir interferometry justification

Through a rapid look at (43) it is evident that the multiplicative term of the phase uncertainty is an increasing function of the off-nadir angle. Therefore the attainable accuracy in the determination of surface elevation through interferometric systems can be greatly increased by decreasing the off-nadir angle θ. This basic property is the main reason in the direction of the analysis of interferometric configuration with low off-nadir angle.

The other advantages concern the simplifications which can be introduced in data processing. Firstly the phase of images registration can be surely skipped. In fact the expected translation between the interferometric images (ΔR) mostly depends on the component of the baseline along the slant range direction, which is a decreasing function of the off-nadir angle, as in the following:

$$\Delta R \approx B\sin\vartheta - \frac{B}{2(h-H)}\cos\vartheta \qquad (59)$$

If also low resolution images are required, as it is the case for oceanographic application, a great number of look can be performed, implying significant reduction of the phase variance following (51).

2.6. Backscattering model

For ocean, the off-nadir backscatter cross section is assumed to be given by the specular-point geometrical optics [69], with the stationary-phase approximation. By assuming a Gaussian-distributed random surface with variance σ^2 and a Gaussian correlation function of the form:

$$\rho(\xi) = \exp\left(-\frac{\xi^2}{l^2}\right) \tag{60}$$

where l is the correlation length, different approximation can be considered. The first one is relative to the condition $k\sigma > 2$ that allows to evaluate the following bistatic scattering coefficient for the pq polarisation:

$$\sigma_{pq} = \frac{\left(kq|U_{pq}|\right)^2}{2q_z^4\sigma^2\left|\rho''(0)\right|} \exp\left(-\frac{q_x^2 + q_y^2}{2q_z^2\sigma^2\left|\rho''(0)\right|}\right) \tag{61}$$

where:

$$q_x = k(\sin\theta_s \cos\varphi_s - \sin\theta\cos\varphi)$$
$$q_y = k(\sin\theta_s \sin\varphi_s - \sin\theta\sin\varphi)$$
$$q_z = k(\cos\theta_s + \cos\theta) \tag{62}$$
$$q = \sqrt{q_x^2 + q_y^2 + q_z^2}$$

$\sigma^2 \left| \rho''(0) \right|$ corresponds to the mean-squared slope of the surface;

$k = \dfrac{2\pi}{\lambda}$ is the propagation constant;

U_{pq} are polarisation terms evaluated in [70].

The reference geometry in depicted in Figure 9. The backscattering case means $\theta_s = \theta, \varphi_s = \pi, \varphi = 0$, that gives:

$$\sigma_{pp}(\theta) = \frac{\left| R_{pp}(0) \right|^2}{2\sigma^2 \left| \rho''(0) \right| \cos^4\theta} \exp\left(-\frac{\tan^2\theta}{2\sigma^2 \left| \rho''(0) \right|} \right) \tag{63}$$
$$\sigma_{pq}(\theta) = 0$$

where $R_{pp}(0)$ is the Fresnel reflection coefficient evaluated at normal incidence.

By decreasing the value of surface height variance, coherent scattering arises. In this case ($k\sigma < 2$), a closed form can be given if the surface r.m.s. slope is less than 0.25. Following [71], it is possible to express the bistatic scattering coefficient as a sum of a coherent (σ_{pqc}), noncoherent (σ_{pqnc}) and surface (σ_{pqs}) terms as:

$$\sigma_{pq} = \sigma_{pqc} + \sigma_{pqnc} + \sigma_{pqs} \tag{64}$$

$$\sigma_{pqc} = \pi k^2 |a_0|^2 \delta(q_x)\delta(q_y)\exp(-q_z^2\sigma^2) \tag{65}$$

$$\sigma_{pqnc} = (0.5 \cdot k|a_0| \cdot l)^2 \exp(-q_z^2\sigma^2)\sum_{n=1}^{\infty}\frac{(q_z^2\sigma^2)^n}{n!n}\exp\left[-\frac{(q_x^2+q_y^2)l^2}{4n}\right] \tag{66}$$

$$\sigma_{pqs} = -(k\sigma l)^2\frac{q_z}{2}\exp(-q_z^2\sigma^2)\operatorname{Re}\left\{a_0\left(q_x a_1^* + q_y a_2^*\right)\right\}\sum_{n=1}^{\infty}\frac{(q_z^2\sigma^2)^{n-1}}{n!n}\exp\left[-\frac{(q_x^2+q_y^2)l^2}{4n}\right]$$
$$\tag{67}$$

where the values of polarisation coefficients $a_{0,1,2}$ can be found in [70].

Finally, when both the surface standard deviation and correlation length are smaller than the wavelength, a different method should be used. A standard approach is the small-perturbation method, than can be used if:

$$k\sigma < 0.3$$
$$\frac{\sqrt{2}\sigma}{l} < 0.3 \tag{68}$$

In this case:

$$\sigma_{pq} = 8\left|k^2\sigma\alpha_{pq}\cos\theta\cos\theta_s\right|^2 W\left(k_x + k\sin\theta, k_y\right) \tag{69}$$

where the polarisation terms α_{pq} are defined in [70] and $W(u,v)$ is the Fourier transform of the surface correlation coefficient, that, in case of Gaussian distribution, it is given by:

$$W(u,v) = \frac{l^2}{2}\exp\left(-\frac{u^2+v^2}{4}l^2\right) \tag{80}$$

For typical ocean conditions, the parameters involved in the scattering model can be derived from the altimeter wind speed model function of [72], in which the global wind speed distribution is approximated by a Rayleigh distribution with a mean 19.4 m/s wind speed of 7.4 m/s.

From [72] it is possible to use the nadir incidence model function in order to estimate the effective slope variance as a function of wind speed.

For the median (7m/s wind speed) and 90-percentile (14.5 m/s wind speed) conditions correspond a surface mean-squared slope of 0.0246 and 0.0320 respectively.

The other parameters are shown in Table 1 and the evaluated ocean backscattering as a function of the incidence angle is shown in Figure 10.
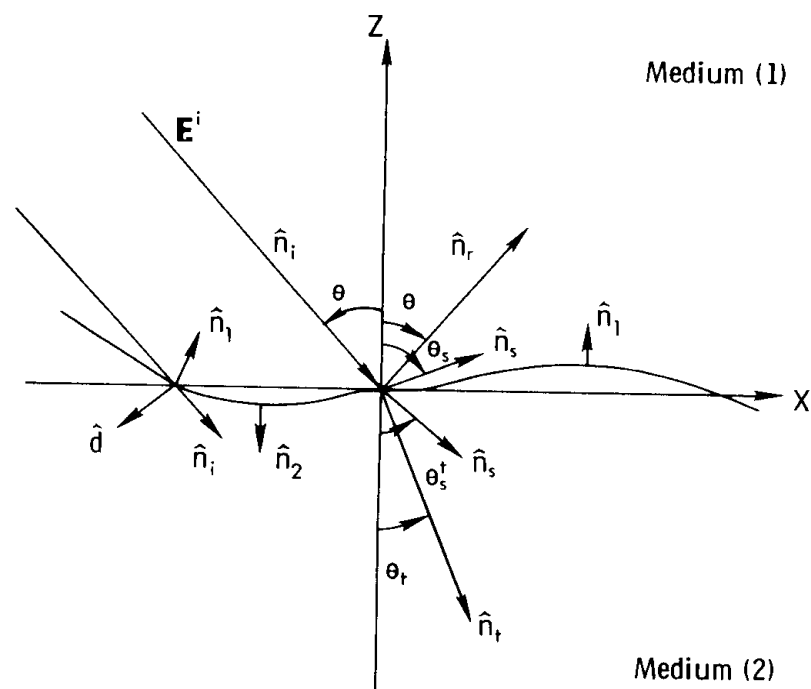
Figure 9 – Reference geometry for surface-scattering problem

Wind speed [m/sec]	7	14.5
Mean-squared slope	0.0246	0.0320
Correlation length [cm]	9.0	7.9
Dielectric constant	70	
Height rms [cm]	1	
Operating frequency [GHz]	9.65	
$k\sigma$	2.0	
$\left| R_{pp}(0) \right|^2$	0.6	
Model used	Eq. (63)	

Table 1 – Parameter for ocean scattering evaluation
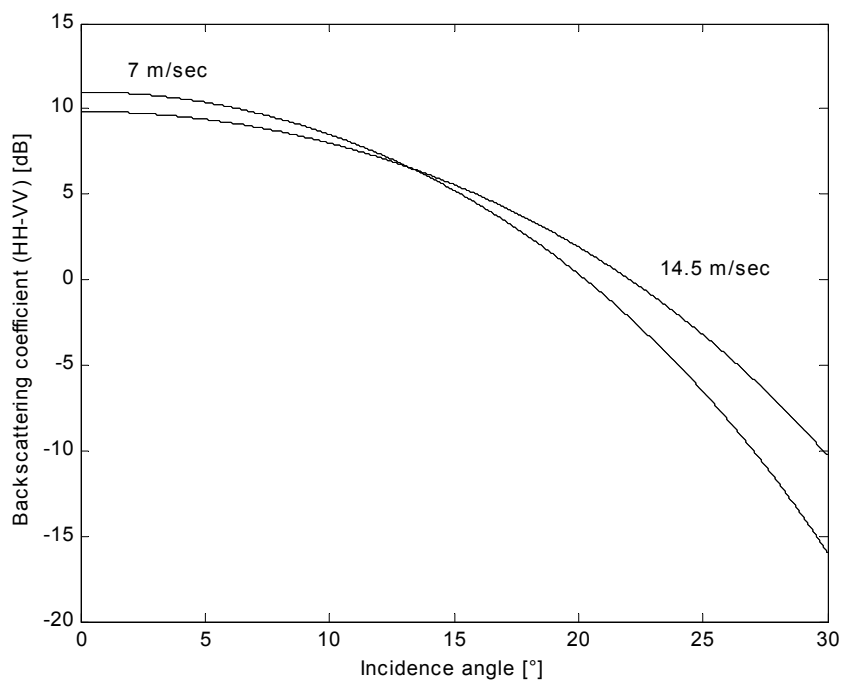
Figure 10 – Ocean backscattering as a function of incidence angle

Before concluding this paragraph, we want to note that radar cross section has got a strong angular variation, which is function of wind speed and direction and the challenge of predicting the angular and spatial variation from the altimeter data alone with an accuracy sufficient for obtaining centimeter level height accuracy is impossible to meet. Nevertheless this problem, which is present in what we can call "amplitude interferometry", can be overcome if we use the interferometric phase alone to misure the topography, independent to to the signal amplitude[65].

2.7. Brief Review of the most important formula used in the simulation model

In order to design a preliminary near-nadir interferometry, only phase (ϕ) and roll (α) errors have been taken into account in this analysis.

The following simplified expressions have considered:

$$\sigma_h = \sqrt{\sigma_{h,\phi}^2 + \sigma_{h,\alpha}^2 + \sigma_{h,Bx}^2} \tag{70}$$

$$\sigma_{h,\phi} = \frac{\partial h}{\partial \Phi}\sigma_\phi = \frac{(H + r_e)}{r_e} \cdot \frac{R \, \text{sen} \, \theta}{2k(B_y \cos \theta - B_z \cdot \text{sen} \, \theta)}\sigma_\phi \tag{71}$$

$$\sigma_{h,\phi} = \frac{\partial h}{\partial B_x}\sigma_{Bx} = \frac{(H + r_e)}{r_e} \frac{B_x \, \text{sen} \, \theta}{(B_y \cos \theta - B_z \cdot \text{sen} \, \theta)}\sigma_{Bx} \tag{72}$$

$$\text{SNR} = \frac{P_{av} G^2 \lambda^2 \rho_{gr} \rho_x \sigma^0(\theta)}{(4\pi)^3 R^4 N L_s L_a} \qquad (73)$$

$$\sigma_{pp}(\theta) = \frac{|R_{pp}(0)|^2}{2\sigma^2 |\rho''(0)| \cos^4 \theta} \exp\left(-\frac{\tan^2 \theta}{2\sigma^2 |\rho''(0)|}\right)$$

$$(74)$$

On the basis of the simple models shown in previous paragraphs, it is possible to define the main system parameters and assess its performance, in terms of resolution and final height uncertainty.

After a preliminary trade-off analysis, based also on sub-system feasibility given by the current technology, the system parameters shown in Table 2 have been determined.

It is worth noting the following main points:

- the choice of the transmitted frequency value (X–band) is due to allow the installation on board of a nadir-pointing altimeter working in S and Ku band (RA-2 like) for calibration purposes;

- the values of peak power and transmitting bandwidth are the state of the art of the current technology;

- the baseline is supposed to be directed only along the cross-track direction (y-axis);

- the antenna size has been derived by considering an uniform illumination;

- the needed value of roll uncertainty (0.05 arcsec) is surely not feasible. It is two

or three order of magnitude smaller than the values provided by the current satellite attitude control systems. This value has been inserted only as a reference for evaluating the final height error and the procedures for calibrating the errors induced by the actual uncertainty in the knowledge of satellite roll will be discussed in following dedicated paragraphs.

The results obtained by the performance analysis for ocean mode are shown in Figure 11.
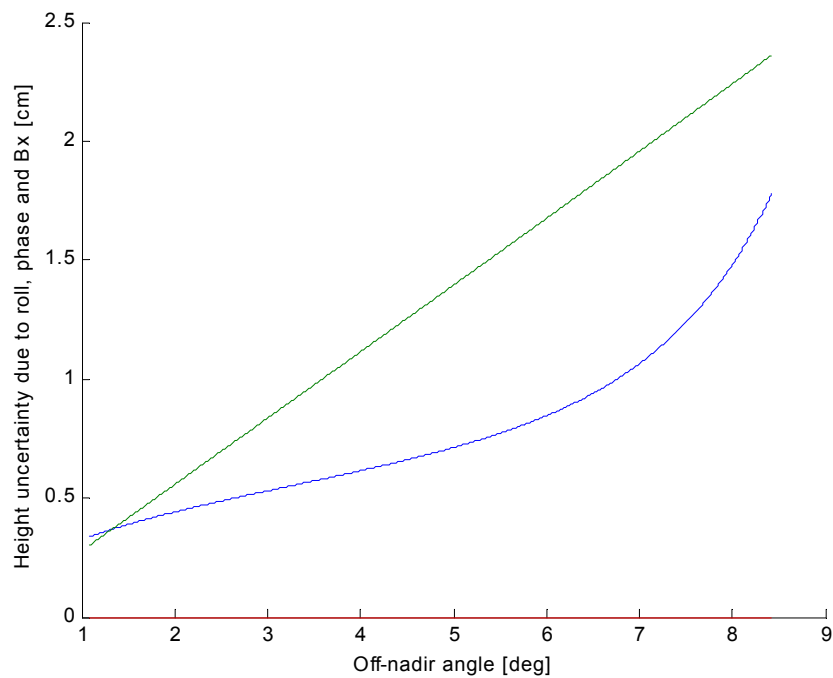
Figure 11 – Component of height uncertainty as a function of off-nadir angle (ocean mode)

(blue=phase, red=Bx, green=roll)

	OCEAN MODE Double swath No ping-pong
Satellite altitude [Km]	600
Operating frequency [GHz]	9.6
Transmitted bandwidth [MHz]	200
Transmitted peak power [W]	300
Receiving bandwidth [MHz]	200
Sampling frequency [MHz]	480
Along-track antenna dimension [m]	2.5
Across-track antenna dimension [m]	0.2
Antenna efficiency	0.6
Antenna pointing [°]	+/- 5
Baseline length [m]	10
Noise figure [dB]	4
System losses [dB]	3
Atmospheric losses [dB]	1
Required azimuth resolution [Km]	10
Required ground range resolution [Km]	10
Roll uncertainty [arcsec]	0.05
Pulse duration [μsec]	68
PRF [KHz]	8
Burst length [msec]	4
Number of pulses per burst	32
Swath [Km]	77.6
Acquisition time per pulse	115
Minimum ground range (wrt satellite track)	11.3
Maximum ground range (wrt satellite track)	88.9

Table 2 – Main system parameters

CHAPTER III

CALIBRATION PROCEDURES: THE UNCERTAINTY

INTRODUCED BY THE ROLL

1. Introduction to the problem

As shown in the previous paragraph of the preceding chapter the real problem is the roll error that gives the main contribution to the final height uncertainty. The effects of the other parameters involved in the total height accuracy can be kept very low by the actual technology.

Given the look direction θ, the surface height h and the cross-section position x, relative to a tangent plane at the centre of the swath, are given by:

$$h = H - r_0 \cos \vartheta \tag{75}$$

$$x = r_0 \sin\theta \tag{76}$$

where H is the height of the platform above the tangent plane. Differentiating (75) and (76) with respect to the baseline roll angle, one find that an error in the baseline roll angle $\delta\alpha$ introduce a tilt error on the estimated height:

$$\delta h = r_0 \sin\vartheta\delta\alpha = x\delta\alpha \qquad\qquad\qquad (77)$$

Due to the long range for spaceborne instruments, the requirement on the baseline roll knowledge is very stringent, As an example, a 1 arcsec baseline roll error translate into 48 cm error at a cross track distance of 100 km. Therefore, to obtain 5 centimetre accuracy or better over the entire swath, the baseline roll must be known to within at least 0.1 arcsec. This level is currently beyond the capability of the best star tracker, as shown in the next section.

Figure of 0.05 arcsec is necessary to keep the total height arror below 3 cm over the whole swath, as shown by Figure 11.

2. The star tracker solution and its inadequacy

In the next pages are reported the analysis done for evaluating the possibilities of using star-tracker for measuring the roll angle.

2.1. Operating principles of a star tracker

An autonomous star tracker is an avionics instrument used to provide the absolute 3-axis attitude of a spacecraft utilising star observations. Basically, a star tracker is an electronic camera connected to a microcomputer that includes a mathematical model of the spacecraft motion, accurate enough to extrapolate the attitude. Using a sensed image of the sky it automatically performs pattern recognition of the star patterns in the field of view (FOW) and calculates the attitude with respect to the celestial sphere; stars, infect, can be located and identified by the processor which has the capability to perform star identification utilizing an internal star catalogue stored in firmware and to calculate the attitude quaternion (=the orientation of the spacecraft) autonomously. Based on the celestial coordinates of the identified stars, it is possible to calculate the celestial coordinates of the centre of the image and the rotation around it. The centre of the image is the same as the pointing direction (PD) of the camera. With the PD and with the knowledge of how the camera is mounted on the spacecraft body, it is possible to calculate the attitude of the spacecraft.

An autonomous star tracker typically operates in two modes: 1) initial attitude acquisition and 2) tracking mode.

In the initial attitude acquisition mode the instrument recognizes the stars form the pattern they form. There has been published a variety of algorithms for patterns recognition, a typical example is that reported by Liebe.

A star catalogue is constructed so that there are 20 stars in the FOV on average. For all stars in the sky the angular distance to the first and the second neighbour star is registered. A star is then registered by:

a) The angular distance to the first neighbour star.

b) The angular distance to the second neighbour star

c) The spherical angle between the two neighbour stars.

Typically, the identification can be accomplished in few seconds.

Normal operating mode (tracking mode), instead assumes that the present attitude is close to the last attitude updates (~ less than 1 s ago). The task is much easier since the star tracker only has to track previously identified stars at known positions. Attitude and rate information from previous exposures is used in tracking mode to predict star positions in the next exposure. Therefore, it is not necessary to digitize the entire image. Some star trackers utilize special hardware that only digitizes specific small windows in the image at predict star positions. The positions of star centroids on the focal plane can be transformed into unit vectors in a star tracker based coordinates system. The unit vectors of stars in an inertial based coordinates system are also known from the firmware star catalogue. The average rotation

(usually calculated using quaternion mathematics) from the inertial based coordinates system to the star tracker based coordinates system can therefore be calculated: the output of an autonomous star tracker is, thus, often a quaternion, but could be a direction cosine matrix or Euler angles, too.

2.2. Accuracy of a star tracker

The average number of stars in the FOV and the brightness of the stars are very important to the accuracy (as we'll see at the end of this paragraph), so now we calculate star light sensitivity, determine star detection threshold and give equations to determine the average number of stars in the FOV.

Star light sensitivity

Many bright stars in the sky have surface temperatures close to that of the Sun. The Sun has an apparent magnitude of M_V= -26.7 and the solar flux is 1.3 Kw/m^2.

Therefore the Sun is $2.5^{26.7}$= $4.2*10^{10}$ times brighter than a magnitude 0 star. The incident energy from a magnitude 0 star on an area of 1 mm^2 has the same relative spectral characteristic as a black body radiator, so the total power is: (1.3 Kw/m^2* 10^{-6}m^2)/ $4.2*10^{10}$= $2.96*10^{-14}$ W/m^2. The radiation from a black body is:

$$I(\lambda,T)=(2*\pi*h*c^2)/\lambda^5*(e^{h*c/\lambda*k_b*T}-1) \qquad (78)$$

The absolute spectral characteristic of the influx is found multiplying a constant to (78) so the total power is $2.96*10^{-14}$ W/m^2. Typically star trackers restrict the wavelengths that reach the focal plane (optical system typically transmits wavelengths in the 400- 800 nm band).

It is possible to express the power influx in terms of photons/s by dividing the power influx by photon energy ($E = h*c/\lambda$). The fraction of photons that are converted into photoelectrons on the focal plane is called the absolute quantum efficiency (QE). The QE is multiplied with the photon influx. The result of summing over the wavelengths (using the QE of a typical silicon focal plane array) is 19100 photoelectrons, which means that a star tracker which has an exposure time of 1 s and a lens of 1 mm² will generate 19100 photoelectrons for a magnitude 0 star of spectral class G2. As an example, a star tracker has a 3 cm lens aperture and a 200 ms exposure time. It images an M_V=4 star, then it generates:

19100 photoelectrons/s*mm^2 $\cdot 1/$ 2.5^4 $\cdot$ 0.2 s/exposure $\cdot$ π $\cdot 15^2$ mm^2 = 69235 photoelectrons/exposure $\qquad\qquad\qquad\qquad$ (79)

This formula shows that the number of photons from a star is finite.

<p style="text-align:center">Star detection threshold</p>

The principal contributions to the signal noise are typically: read noise, dark current noise, inhomogeneity of the dark current. It is possible to estimate the background noise as the standard deviation of all pixel values in a dark frame. A focal plane consist of 10^6 pixels and it is therefore reasonable to set the detection threshold for a

star signal to be the average background pixel value + 5 times the standard deviation. A star is detected if the brightest pixel in the star is above the threshold. The brightest pixel depends on the point spread function (PSF).

$$\text{detection limit} = A_{pixel} + 5 \cdot \sigma_{pixel} \cdot 1/\int_0^1 \int_0^1 1/(2 \cdot \pi \cdot \sigma_{PSF}) \cdot e^{-x^2 + y^2/2 \cdot \sigma}{}_{PSF} \, dx \, dy \qquad (80)$$

where A_{pixel} is the mean value of the pixel and σ_{pixel} is its standard deviation in the dark frame and σ_{PSF} is the PSF radius in pixels (assuming a Gaussian PSF).

Average number of stars in the FOV

It is assumed the FOV is circular and is A deg wide. The fraction of the sky that is covered by the FOV is :

$$(1 - \cos(A/2))/ 2 \qquad (81)$$

The number of stars brighter than a given magnitude can be estimated by the following relationship for the PPM star catalog:

$$N = 6.57 \cdot e^{1.08M} \qquad (82)$$

Where M is the magnitude. The average number of stars in the FOV is :

$$N_{fov} = 6.57 \cdot e^{1.08M} \cdot (1 - \cos(A/2))/ 2 \qquad (83)$$

Using a general catalogue the N_{fov} can be calculate with the following formula:

$$N_{fov} = \text{number of stars in the catalog} * (1 - \cos(A/2))/ 2 \qquad (84)$$

Ideally a star tracker should be able to operate at all attitudes, but two stars must, as a minimum, be present in the FOV to calculate the attitude solution. Unfortunately stars are not homogeneously distributed in the sky, therefore there are areas on the sky, where there are not enough stars for star trackers to operate.

It should be noted that 2 is the theoretical limit to operate, but normally a star tracker requires more than 2 stars in the FOV and much more stars in the initial acquisition mode.

Hyperacuity

The angular resolution of a pixel in a CCD chip is

$$\zeta = \frac{2\theta}{N_{CCD}} \qquad (85)$$

where θ is the half opening angle of the lens and N_{CCD} is the number of pixels in the CCD. Typically a CCD chip contains $300 - 1000$ pixels in each direction and θ is $3°$ - $20°$. It is evident that the desired accuracy can't be obtained directly.

There are three ways to increase the accuracy:

1. Supixel precision

2. All the stars in the image can be used to calculate the attitude. The increase in the accuracy is obtained by statistical means

3. The attitude calculation can based on more than one star image. Statistical properties will again increase the accuracy.

The most used technique is the hyperacuity (= sub pixel precision).

In a focused image a star appears as a point source, so all the photoelectrons from a star are generated in a single pixel. However if the image is defocused slightly a star will occupy several pixels. This facilitates to model the centre of the stars mathematically with subpixel accuracy. It may seem intuitively inconsistent with the sampling theorem to increase the accuracy beyond one pixel, but it is the a priori knowledge of the PSF that is utilized in combination with the actual measure. The performance of the hyperacuity technique is determined by the algorithm used to determine the centre of the star. Some authors claim to achieve subpixel precision better than 1/100, others in order of 1/10 (1σ) pixel, all depends on the S/N ratio.

An image acquired with a star tracker includes many stars. If the hyperacuity technique can determine a star position with accuracy of e_{star}, the accuracy of PD is:

$$\varepsilon_{PD} = \frac{\varepsilon_{star}}{\sqrt{N_{FOV}}} \tag{86}$$

More precisely we can say the most important error in the star tracker is the NEA (or PD- error). It is the star tracker's ability to reproduce the same attitude provided the same optical simulation. This error consists of photon noise, dark current noise, read/amplifier noise, limited resolution of the A/D converter. It is possible to estimate it with the following expression:

$$\varepsilon_{PD} = A \frac{\varepsilon_{centroid}}{N_{pixel} \sqrt{N_{FOV}}} \tag{87}$$

Where A is the Fov angular aperture and $\varepsilon_{centroid}$ is the average centroid accuracy (for example 1σ). As an example, a star tracker has got 512 * 512 pixels, a FOV of 15°. The star centroid noise is 1/10 and there are on the average 20 stars in the FOV. The NEA is:

$$\frac{15° \cdot 0.1 \text{pixel}}{512 \cdot \sqrt{20}} = 2.3 \text{ arcseconds.} \tag{88}$$

The accuracy of the rotation around PD is less accurate, typically 4 – 20 times worse than the PD's one (see reference 2 for details), but for our scopes only the accuracy of the PD is important.

In few words the accuracy ca be expressed as:

accuracy = f(FOV, Star catalogue size, CCD chip, Hyperacuity routine)

The engineer is faced with the problem of optimizing these parameters to achieve the best performances. Unfortunately the parameters are not independent.

FOV

The FOV is the most important one.

A little FOV implies an easy design of the camera lens and high accuracy. However, as the FOV decreases initial acquisition of the attitude becomes more difficult and the size of star catalogue grows to prohibitive sizes.

Number of Stars in the Catalogue

It is desirable to have many stars in the image, because it increases the accuracy and it simplifies the pattern recognition. The stars emit a limited amount of photons and a CCD camera has a limited QE (as we have seen), therefore, there are only two parameters to determine the sensitivity of the system: the design of the camera lens and the exposure time.

In order to have many stars in the FOV the aperture must be big. The sensitivity is proportional to the area of the front lens. However, as the front lens increases in size, the weight of the lens increases and the distortion in the lens gets more dominant. This implies that the hyperacuity algorithm performs more poorly.

Increasing the exposure time of the CCD chip we increase the sensitivity of the system. However, the strategy has disadvantages as update rate decreases and the image will include motion smear. Motion smear tends to decrease the performance of hyperacuity technique.

Hyperacuity Technique

There is an enormous range of illumination from the brightest to the dimmest stars. In the digitization of the CCD signal there is a limited resolution ($7 - 15$ bits), this implies that the brightest stars will overflow and the dimmest ones will be difficult to detect due to noise. It is impossible to give an analytic solution to the optimal choice of systems gain/detection level; it depends on the hyperacuity algorithm and the hardware.

2.3.   Conclusions

These instruments are capable of determining the attitude with accuracy better than 1 arcsecond. The ongoing technology development will decrease the power consumption and mass of autonomous star tracker significantly. However, since the number of photons from the star is finite and the parameters from which accuracy depends are not independent and must be chosen carefully using the criterions seen above, no major improvements in the update rate or accuracy is anticipated in the future.

Therefore a fast research on web has been made in order to see the performances of the star tracker produced from some of the most important farms in the space ambit and the results are summarized in the following table. As you can see they are very

far from the measures orders we need for our application. In our opinion this solution is not the right one to resolve the problem of knowing the roll with the desired accuracy of of 0.05 arcsec.

Farm	MODEL	PD ACCURACY	PD Accuracy in arcsec.	Year
OCA	WFOV Star Camera	160 µrad	33	
EMS Space & Technology	CALTRAC	0.005°	18	2001
Ottiche Galileo	A-STR	10 arcsecond	10	
Ball Aerospace & Technology Corp.	CT-633	6 arcsec	6	
Sodern	SED12	2.5	2.5	
Sira Electro-Optics	AST20	5	5	

3.   Nadir looking altimetry

A solution to the problem of roll uncertainty can be represented by the combined application of nadir looking altimetry.

In this case, the height measured by the altimeter at a point with ground co-ordinate x_A is given by:

$$h_A(x_A) = h(x_A) + n_A \qquad (89)$$

where $h(x_A)$ is the true height and n_A is the noise introduced by the altimeter that affects its final uncertainty. Similarly, the height measured by the interferometer can be modelled as:

$$h_I(x_I) = h(x_I) + n_I + \delta_{roll} \qquad (90)$$

where n_I is the noise introduced by the interferometer and δ_{roll} is the error caused by the roll uncertainty. Different points x_A and x_I have been considered in order to take into account that for the particular observation geometry, as it is depicted in Figure 3, the measures are taken by the altimeter and the interferometer in two different points. In other word, we try to correct the measure made by the interferometer by one made by the altimeter in a different point not very far.

The roll error can be estimated by taking the difference between the last two

relations:

$$h_I(x_I) - h_A(x_A) = \Delta h(x_I - x_A) + n_I - n_A + \delta_{roll} \tag{91}$$

It can be easily demonstrated that this estimator is unbiased.

Therefore, the accuracy in the evaluation of the height error by this estimator, due to roll angle uncertainty, can be expressed in terms of the variance of the estimator, σ_{roll}^h:

$$\sigma_{roll}^h(x_I) = \sqrt{\sigma_A^2 + \sigma_I^2 + 2\sigma_h^2[1 - C_h(x_A - x_I)]} \tag{92}$$

where σ_h^2 and $C_h(x_A - x_I)$ are the spatial variance and autocovariance function for the sea-surface height, respectively, σ_A is the accuracy of the nadir-looking altimeter and σ_I is the accuracy of the interferometric altimeter without roll uncertainty.

Given the result of (92) it is possible to evaluate the roll error along the swath by propagating the (92) itself, as suggested by (76):

$$\sigma_{roll}^h(x) = \frac{x}{x_I}\sigma_{roll}^h(x_I) \tag{93}$$

3.1. Performance of the solution

Given the last relation and the behaviour of the interferometric height error of as well as of the autocovariance function. The (92) can be translated in the corresponding roll uncertainty by using the (76), that gives, in our case, about 1 arcsec (it corresponds to an uncertainty of about 45 cm). These figures are 20 times the needed value (0.05 arcsec). This means that we can not rely on a single measurement but it would be necessary 400 independent measurements to reach an adequate roll angle estimate.

The final height uncertainty along the swath is shown in Figure 12. Best results can be achieved by evaluating the (92) at the far edge of the swath and by using relation (93) for correcting the other points within the swath, but as expected the height uncertainty continues to reache unacceptable values (see Figure 13). This is due to the wide swath involved and, mainly, to the fact that the nadir-looking altimeter and inteferometric measurements are not taken within the same resolution cell (i.e. autocorrelation equal to one). The consequence of this is that this technique didn't revealed itself as we expected so, as we'll see in next paragraphs we passed to analyze a different solution.
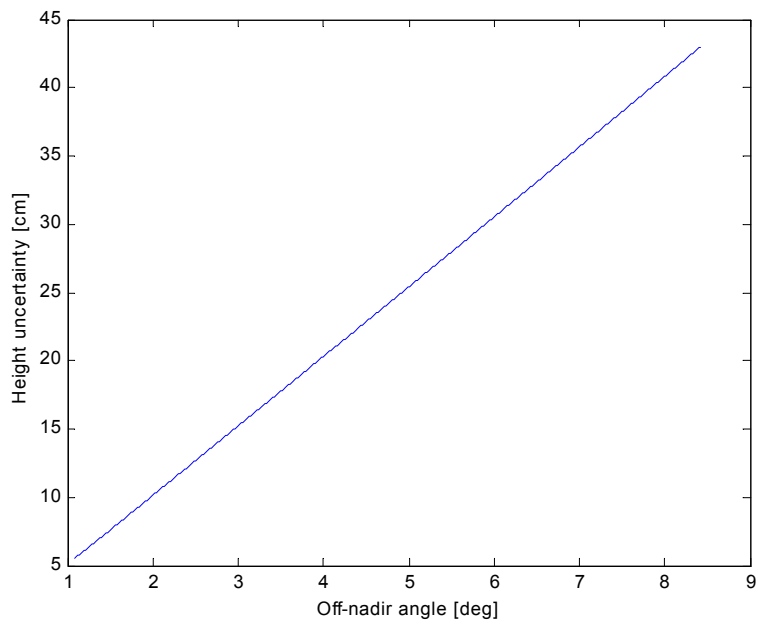
Figure 12 - Final height uncertainty after calibration with nadir-pointing altimeter
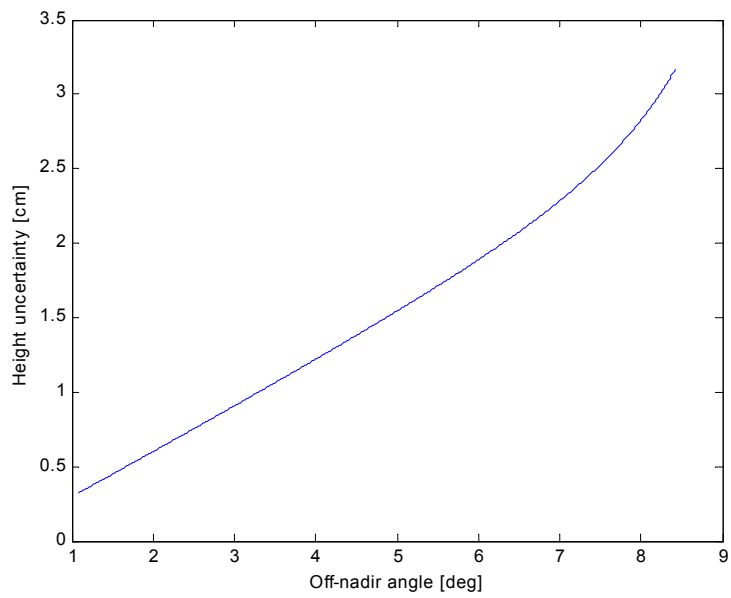
Figure 13 Final height uncertainty after calibration with nadir-pointing altimeter(best case)

3.2. Variance and Covariance evaluation using ra-2 data

3.2.1. Introduction

As we said before, in order to estimate the roll error with nadir-looking altimeter measurements, the spatial covariance of the see is required.

Evaluation of σ_h^2 and $C_h(x_A - x_I)$ are reported in [73] by using TOPEX data, while this thesis shows results obtained with RA-2 data.

RA-2 is the altimeter radar on board of ENVISAT whose technical characteristics can be synthesized in the following table (for more datail see [74]).

Orbit Range (H)	764 - 825 Km
Operative Frequency	13.575 Ghz (Ku) 3.2 Ghz (S)
Pulse Length (τ)	20 µsec
Ku Tx pulse Bandwidth (B_c)	320 - 80 - 20 Mhz - CW
S Tx pulse Bandwidth (B_c)	160 Mhz
Tx Peak Power (P_p)	60 W (Ku) 60 W (S)
Pulse Repetition Interval	557 µsec (Ku) 2228 µsec (S)
Antenna Gain (G_a)	41.5 dBi (Ku) 29.2 dBi (S)
Antenna Beamwidth (θ_B)	1.33 deg (Ku) 5.25 deg (S)
RF Losses (L_{RF})	3.7 dB (Ku) 4.0 dB (S)
Receiver Noise Bandwidth (B_n)	6.4 Mhz
Receiver Noise Figure (F)	4 dB (Ku) 4 dB (S)
FFT Processor	128 points
A/D conversion (no. bits)	8

The RA-2 products (all bits files) are summarized in the following table.

Instrument / mode	Product ID	Description
RA-2	RA2_CAL_0P	RA2 Calibration and BITE Mode Level 0
	RA2_ME__0P	RA2 Measurement Mode Level 0
	RA2_MW__1P	Geolocated and calibrated Altimeter Waveforms with TOA Microwave Brightness Temperatures
	RA2_FGD_2P	FDGDR: Fast delivery Geophysical Data record from RA-2 and Water Vapour/Liquid Content from MWR. Available 3 hours after data acquisition
	RA2_IGD_2P	IGDR: Intermediate Geophysical Data record from RA-2 and Water Vapour/Liquid Content from MWR. Processed off-line and available 3-5 days after acquisition
	RA2_GDR_2P	GDR: Geophysical Data Record from RA-2 and Water Vapour/Liquid Content from MWR. Processed off-line and available 50 days after acquisition
	RA2_WWV_2P	FDMAR/IMAR: Wind/Wave product with height and MWR information for NRT dissemination to Meteocean users (2 products released at different levels of consolidation: FDMAR built from RA2_FGD_2P or IMAR built from RA2_IGD_2P)
	RA2_MWS_2P	SGDR: Sensor Geophysical Data Record from RA-2, Water Vapour/Liquid content from MWR and Individual Uncalibrated Waveforms from RA-2. Available after 50 days from data take.

Ocean parameters estimation is performed via a dedicated on-ground processing algorithm. The processing requires use of auxiliary files. For the following analysis, second level data with RA2_FGD identification, have been used. This files have been produced from Level 1B products by using dedicated auxiliary files.

Auxiliary data required for Level2 processing may include files used in Level1B processing, plus others data files. The table in the next page can provide an idea about the nature of this auxiliary files

Description	Auxiliary File ID
Solar activity data file	RA2_SOL_AX
Pole location data file	RA2_POL_AX
Platform data file	RA2_PLA_AX
Ionospheric coefficients file	RA2_IOC_AX
Mean sea surface height map file	RA2_MSS_AX
Altitude of Meteo grid points file	RA2_MET_AX
Ocean/Ice2 configuration (system) file	RA2_SOI_AX
Ice1 / Sea Ice configuration (system) file	RA2_ICT_AX
Modified dip map file	RA2_DIP_AX
Cartwright amplitudes file	RA2_SET_AX
Ocean tide solution 1 map file	RA2_OT1_AX
Ocean tide solution 2 map file	RA2_OT2_AX
Tidal loading coefficients map file	RA2_TLD_AX
Geoid height map file	RA2_GEO_AX
Ocean depth / land elevation map file	AUX_DEM_AX
Slope model for Greenland map file	RA2_SL1_AX
Slope model for Antarctica map file	RA2_SL2_AX
RA2 characterisation data file	RA2_CHD_AX
RA2 constants file	RA2_CST_AX
Sea state bias table file	RA2_SSB_AX
ENVISAT-1 Attitude data file	AUX_ATT_AX

Of course these additional data are indispensable for a good interpretation of RA-2 data.

The estimated range measurements are not corrected for the various geophysical effects during the second level processing, but only calculated and supplied in the product.

FGD files consist of a series of records, each representing approximately 1 second of data (precisely 1.114s). In every file FGD there are a number of records relative to

half orbit observation, covering approximately a zone which goes from pole to pole. FGD is processed using DORIS Navigator orbit estimation and is available from PDHS 3 hours after data acquisition. PDHS is the server of Kiruna. They are also available by other servers as that of ESRIN in Frascati, but their files are not completed, since some fields are not available after processing performed by their software, which is different from that in Kiruna.

The FGD structure is :

MPH
Level 2 - SPH
RA-2 MDS
MWR MDS

Where:

I.   MPH and SPH are ASCII headers

II.   RA-2 MDS is composed of several MDSRs (1 MDSR every 1.114 s). MDSRs are the records we have mentioned above. Every MDSR contains different fields, every one correlated to a particular numeric information.

Just to have an idea, we show below a portion of MDSR format:

	Orbit Information				
9	Altitude of CoG above reference ellipsoid	mm	4	ul	1
10	18 Hz altitude differences from 1 Hz altitude [20]	mm	40	ss	20
11	Instantaneous altitude rate	mm/s	2	ss	1
12	Spare (Note 4)	-	50	uc	50
	Range Information				
13	18 Hz Ku tracker range referenced to the COG (no Doppler correction) [20]	mm	80	ul	20
14	18 Hz S tracker range referenced to the COG (no Doppler correction) [20]	mm	80	ul	20

3.2.2. Description of the procedure we used to evaluate covariance and variance

A dedicated Matlab program has been developed, in order to extract from the FGD file the needed information, skipping a certainty number of fields:

1. The height measured by RA-2 (the mean value in a region where it have taken 20 samples)

2. The height of the satellite as regards the reference ellipsoid

3. The geoid height as regards the reference ellipsoid

4. The latitude and longitude of the centre of the region in which we are considering the sample

5. corrections due to the presence of atmosphere, which introduce delays in the signal received by the radar and tides. In particular:

   a.   Model dry tropospheric correction

   b.   Model wet tropospheric or, when it is available, the MWR wet tropospheric correction which is better

   c.   Ionospheric correction

   d.   Inverted barometric correction

   e.   Ocean tide

   f.   Flag for the type of surface (ice, sea etc.)

To have an idea of the order of magnitude of the corrections mentioned at point 5 we can see the Figure 14.
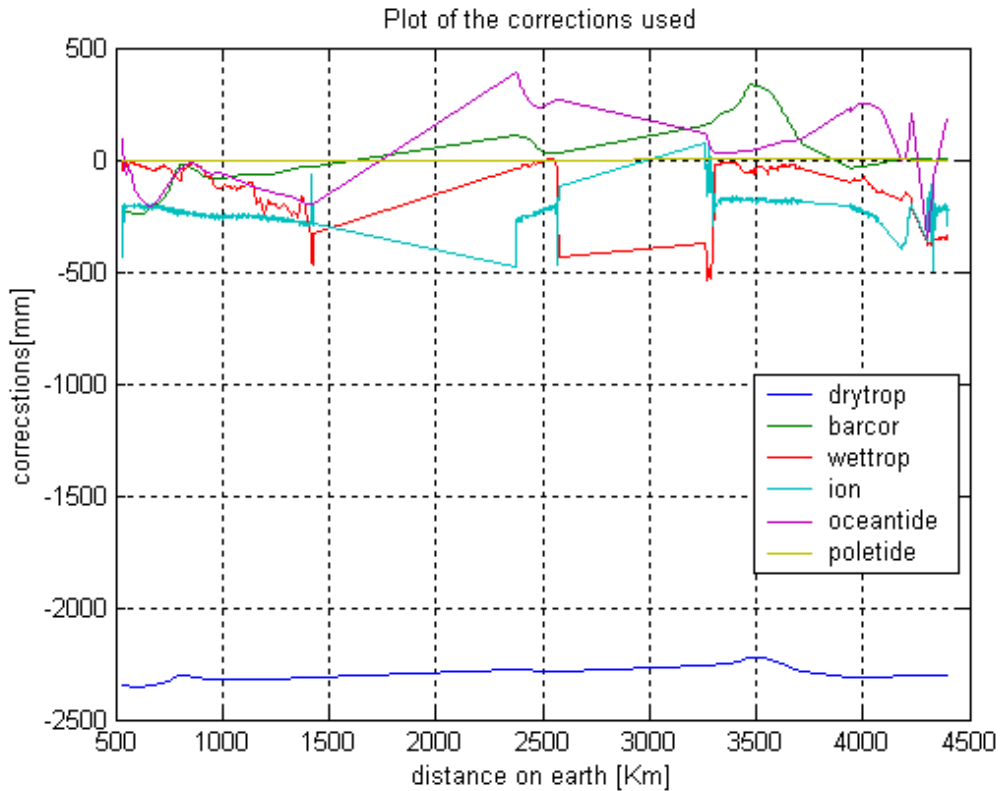
Figure 14 - Corrections due to presence of atmosphere and tide

It's evident that the great part of the introduced corrections are of the order of centimetre except the dry tropospheric correction which reaches values of about 2.5 mt.

Height of satellite minus height measured by RA-2 gives the height of the sea as regards the ellipsoid.

To have a more useful data we have to consider the height of geoid as regards the ellipsoid. In this way what we have is the height of the sea relatively to the geoid. In

a first time this correction was not made and data variability was enormous, because geoid varies as regards ellipsoid from +90 meters to −104 meters, so what we saw was the variability of it as to ellipsoid and not the height of the sea. The final data we used to find the covariance function is:

$$h_{sea} = h_{sat} - h_{ra2} - h_{geoid} - corrections \qquad (94)$$

Every FGD file, as seen, contain half orbit data divided in records. Our program extracts from every file the preceding data for every record. It considers only data from records which are far from the boundaries zones between sea and ice (70 km far), because in those zones satellite doesn't recognize the difference and sees as sea what is ice creating peaks in the final height aspect, showing an increasing sea height where there isn't (80 meters waves appear, clearly unrealistic). Thanks to a program of ESA, ENVIEW (it can help in a fast reading of the FGD files), we controlled that those zones of pecks corresponded to boundaries zones and decided to neglect these data via a latitude control, infect it wasn't an heavy loose, considering that 70 km are nothing compared to the extensions of oceans about which we have data.

ENVIVIEW allows an easy access to the records of the file and a graphical visualisation of the orbit trace on ground and graphical visualisation of the trend of a single variable, but doesn't allows an easy extrapolation of multiple data as we wanted to make averages and to value the covariances. It explains why we have need to develop an our program that did it.

Established on how many kilometres we want to know the aspect of covariance, it is converted in consecutive records the program must consider by the consideration that the distance between a sample and another is 1.114 sec and that the satellite has got a velocity of 7.412 km/s.

$$N_{records} = int(\frac{cov\ lun}{vel_{sat.} \cdot t_{samp}})\qquad\qquad(95)$$

where int is integer part considered for excess.

Therefore, the program consider only data which correspond to sea zones covered by a number of records at least equal to $N_{records}$. We can call this block of consecutive samples «elementary block».

Extracted all the data, on every elementary bock it considers the covariance and the variance.

They are processed by a very simple filtering process: calculated the average value, the program neglects all the values which are grater than two time the mean.

At the end it make an average on al the blocks. These data are stored in a file *.dat, so we can reuse them to make the average on all the files FGD in our possession and calculate the averaged spatial covariance.

At the moment we processed only 6 files, but the data we obtained are very good, so we can imagine that processing more it will be better and better.

We have made a lot of proves considering covariances for zones of different

amplitudes, but at the end we decided to consider in our model the covariance curve for an extension of 200 kilometer. Considering that the swath for the interferometry has an extension of 100 kilometers, a covariance over a zone large two times it appeared a reasonable choice. See Figure 15 for the result. It looks like that presented by Stammer[73] before the elaborated filtering process he makes to the data of TOPEX/Poseidon to remove noise from the signal. Considering he used data over a period of 3 years and we only six files over a period of a month we can say our result is satisfactory.

For the variance σ_h^2 a value of 0.126 m^2 has been evaluated.

To utilize this curve in the program which calculates the height accuracy we made of it a polynomial fitting of the fifth order, which is based on the least squares. The result was a curve identical to the original, but expressible in an analytical form.
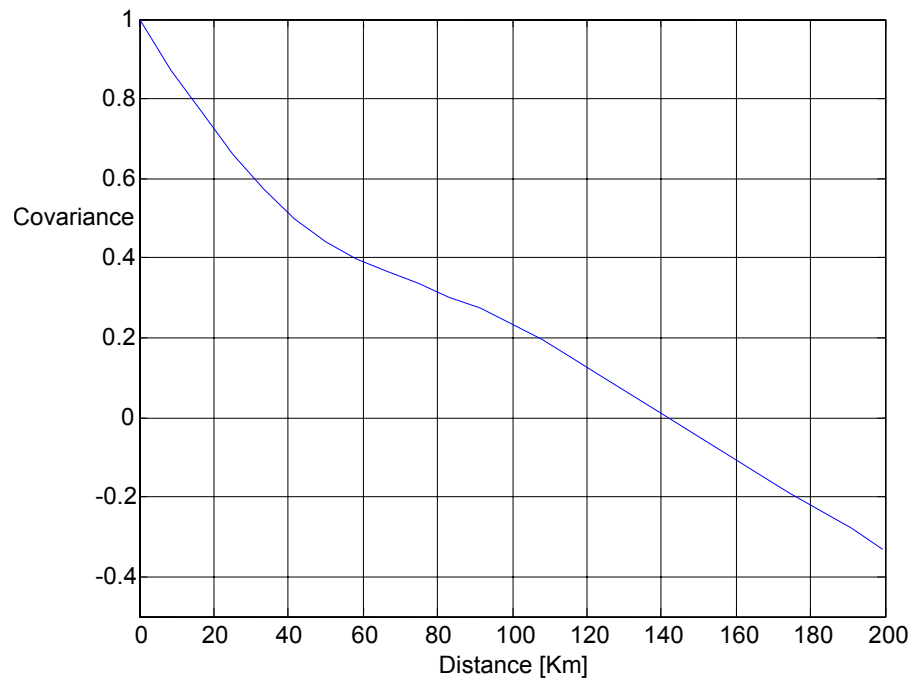
Figure 15 – Autocovariance function of the sea surface height by using RA-2 data

4. The cross over solution

The poor results of the previous calibration method are also due to the fact that only one point can be used for estimating the roll angle. Instead, with the present technique, a great number of resolution cells can be compared and the roll can be assessed with high degree of accuracy. We reduce the height errors introduced by the attitude of the spacecraft, through the interferometer-interferometer cross-overs measurements, which are available in the overlap regions of cross-overs of the ascending and descending orbits. This technique, therefore, uses measurements collected during different days to estimate the platform roll. It is assumed in the inversion that the ocean changes in the time interval between cross-over visits will not significantly impact the ability to measure roll.

The estimated roll angle induces an height error that, then, is removed from the measurements for each swath to obtain estimates of the topography.

After roll error removal, the ocean topography represents the topography at the time of the measurement (with some measurement errors); therefore, although we use data separated in time to perform the calibration, the temporal sampling of the ocean signal is not compromised.

An analysis of cross-over for the considered orbit can be found in [75], where it is shown that after the repeat cycle of 11 days the coverage is almost global as shown by

Figure 16. In addition, within the repeat cycle, also the maximum interval between cross-over

has been analysed.

Figure 17 shows that a good coverage is also reached even if 5 days are considered as the maximum time between the passes that originate the cross-over. This analysis is useful to take into account the right time decorrelation in the calibration procedure. We can have an idea of the geometry involved in this technique considering Figure 18.

At each cross-over point, the ascending (A) or descending (D) interferometer measurements, can be modeled as:

$$h_I^{A/D}(r, t_{A/D}) =$$
$$h_0(r, t_{A/D}) + C_{A/D} \delta \alpha_{A/D} + C_{A/D} S_{A/D} \delta \dot{\alpha}_{A/D} + n_I^{A/D}(C_{A/D}) \tag{96}$$

where $S_{A/D}$ and $C_{A/D}$ are coordinates in the along and across-track directions, respectively, $h_0(r, t_{A/D})$ is the true sea surface height measured at location r and time $t_{A/D}$ and $n_I^{A/D}(C_{A/D})$ represents the interferometer measurement noise, which is a function of the cross-track coordinate alone and is independent between resolution cells.
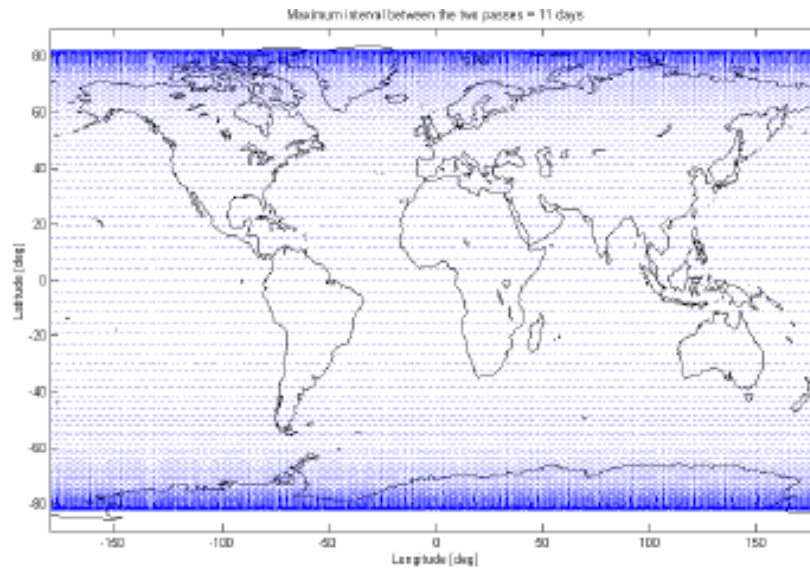
Figure 16 – Cross-over points distribution after a repeat cycle of 11 days
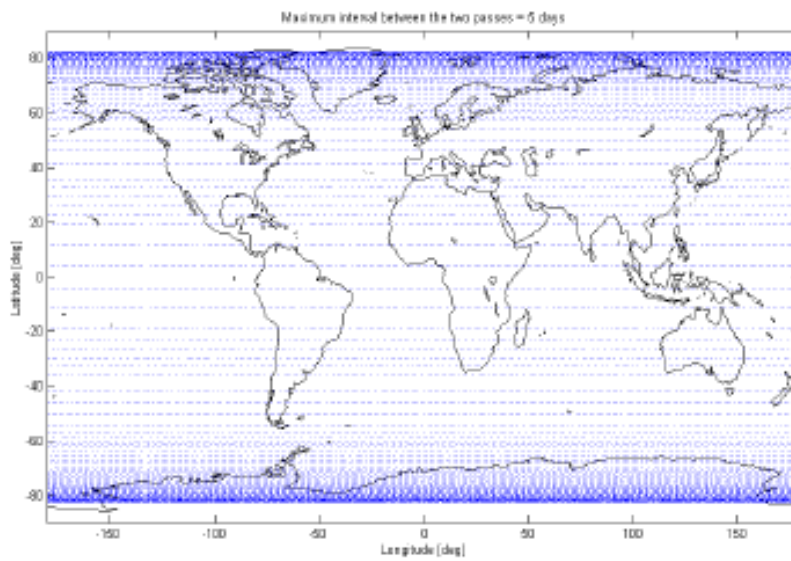
Figure 17 -Coverage analysis of cross-over points within the repeat cycle with 5 days of

maximum time between passes
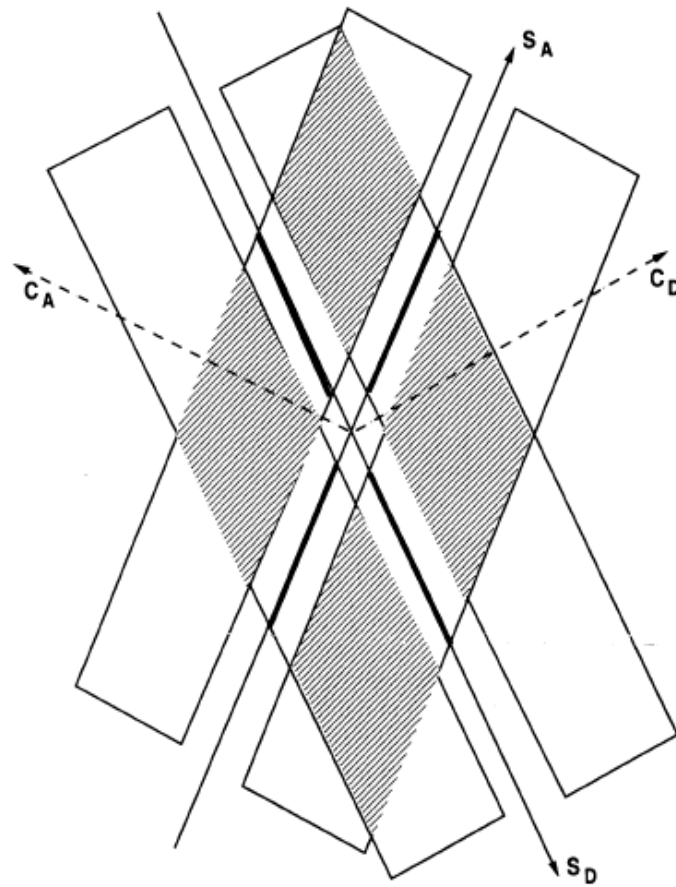
Figure 18 – Geometry involved in cross-over calibration technique

In modeling the systematic error, it is assumed that in the interval between cross-over points the roll error can be assumed to vary linearly:

$$\delta\alpha_{A/D}(S_{A/D}) = \delta\alpha(0) + \delta\dot{\alpha}_{A/D}\, S_{A/D} \tag{97}$$

Under most space-borne circumstances, this is a reasonable assumption given the

slowly varying environment in space on time-scales on the order of one minute, and the short times spent in cross-over diamond, which are on the order of half a minute. The height difference at the overlap regions is:

$$\Delta h_{II} = C_A \delta \alpha_A + C_A S_A \delta \dot{\alpha}_A - C_D \delta \alpha_D - C_D S_D \delta \dot{\alpha}_D + N_{II} \qquad (98)$$

These equations can be inverted, by using maximum likelihood estimation, about which we'll speak in the next paragraph, to estimate the roll error parameters, $\delta \alpha_{A/D}$ and $\delta \dot{\alpha}_{A/D}$. To estimate the roll error parameters by maximum likelihood estimation, it is required that the statistics for the "noise" terms, N_{II}, be known. N_{II} have contributions due to the random measurement noise and to changes in the sea surface height between passes:

$$N_{II} = h_0(r, t_A) - h_0(r, t_D) + n_I^A - n_I^D \qquad (99)$$

The instrument measurement errors are assumed to be zero-mean Gaussian random variables, uncorrelated from point to point, and between instruments. Their standard deviations are given by $\sigma_I(C_{A/D})$.

The ocean surface variability is spatially and seasonally varying, but we assume that, over the short time and spatial scales used for the cross-over calibration, it can also

be treated as a homogeneous correlated Gaussian random process whose statistical characteristics are determined by a spatially varying height standard deviation, σ_0, and a time correlation function, $C(|t - t'|)$.

N_{II}, so, as we have seen, can be considered an addition of Gaussian random variables. Theory assures us that a sum of Gaussian variables is still Gaussian. After some mathematics we found that :

$$\sigma_h^2 = 2\sigma_0^2(1 - C(t_D - t_A)) \tag{100}$$

where $C(t_D - t_A)$ is the normalized covariance of the sea height we have calculated as we explained in the next paragraph. Since interferometer measurement noise and sea heights are Gaussian process uncorrelated we can express the variance of N_{II}, σ_T, simply as the sum of the variances

$$\sigma_T = \sqrt{2\sigma_I + 2\sigma_0^2(1 - C(t_D - t_A))} \tag{101}$$

It appears clear, therefore, why it's important to calculate the temporal covariance of the sea

4.1. Performance of the solution

The only assessment of the cross-over calibration accuracy is contained in a unpublished work of E. Rodriguez and F. Li, where an ocean circulation model of the Atlantic has been used. The basic assumption is that there is no overlap between cross-over regions so that each set of fitting parameters is estimated independently. In practice, the amount of overlap can be substantial, so that this work underestimates the accuracy with which the calibration parameters can be inverted. In addition, the ocean correlation function is assumed to be Gaussian, with a correlation time of 11 days, obtained from the entire simulated data set.

The results indicate that baseline roll can be measured consistently better than 0.1 arcsec and the roll-rate accuracy is also measured substantially better than 0.01 arcsec/sec.

4.2. Temporal Covariance evaluated using RA-2 data

To evaluate the temporal covariance we have used a method substantially not very different from that showed for the spatial covariance. To estimate this covariance we needed for every point (essentially a cell) in which we could divide the ocean data related to consecutive passages of ENVISAT over it. Considering RA-2 is an altimeter with very narrow beam it was impossible to have for it a global coverage and so to hope to make the best of the cross-overs of the orbits to achieve a

multiple passage over a point before the repeating cycle typical of the satellite. We decided, therefore, to use files related to repeating cycle orbits, because in this way we were sure to have a nearly perfect superimposition of the orbit traces and , so, we guarantee ourselves we have multiple time data for all the points of the orbit. ENVISAT has got a orbital period of 6036 sec. and a repetition cycle of 35 days, this means that to have data related to a consecutive passage of the satellite over a point we have to wait 501 orbits, as it can be derived from the formula below:

$$N_{orb} = \frac{D \cdot N_D}{T_{or}} \tag{102}$$

where D is the duration of the solar day (ENVISAT has got an sun-synchronous orbit), N_D is the number of days of the repeating cycle and T_{or} is the orbital period. Seen that ENVISAT was launched not many months ago, it wasn't impossible to collect a lot of data for every point. Considering, besides, that it is in commissioning phase and so there are still some organization problems it was impossible to have by ESRIN all the files related to all the orbits made from ENVISAT form its launch to ours days (It could be possible by Kiruna, but the times for the request were too long for my thesis), we decided to consider for every point data related to only five orbits, that means a period of 140 days.

We extracted data from all the files with all the correction we have seen for the spatial correlation and stored it in a matrix of 3 columns, the first one there were the heights of the see, in the second latitude and in the third longitude of every point.

Constructed these matrices for every file they were stored in a file *.dat, ready to be read by another program which, making a control over longitude and latitude, constructed for every point a vector of observations. On every vectors we applied the covariance algorithm and than we made an average, whose result can be observed in Figure 19.

Clearly this curve has got a lot of limitations, first of all that it was obtained using a few temporal points and temporal distance from a point and another is 35 days, while for our work ($t_D - t_A$) is of about 3-5 days, but from this curve we can hope, making a fitting to extract informations for the delay time we need.
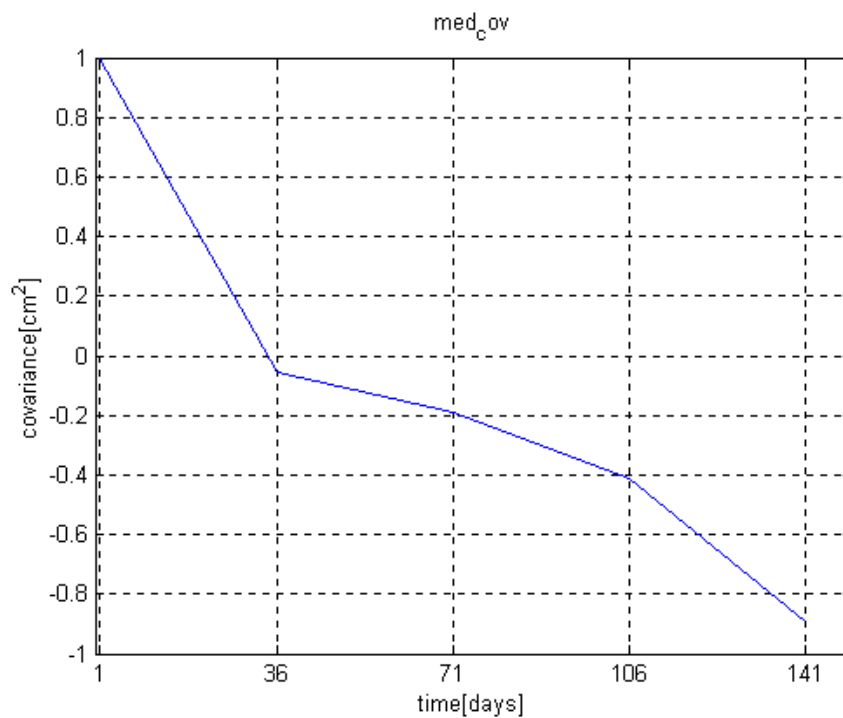
Figure 19 - Correlation curve

This hope come out from the consideration that this curve has got a form not very different from that showed by Stammer in his work mentioned before for one of the four dynamically distinct regions in which he divided the ocean (the energetic boundary currents), it is only more pendent then that of Stammer as it's obvious, because the distance from a point and another is 35 days, so the correlation of the sea after a period so long can be very small.

The form of the curve suggest   that   a possible fitting is an exponential one:

$$f(x) = a \cdot e^{-bx} \qquad\qquad\qquad (103)$$

The parameter b was derived with the least mean technique. The value of a is given by some physical and practical consideration. To be a good approximation of a correlation curve, in the origin, where the delay time is null, it must be 1. This consideration will take us to think that a good value for a is a=1. We, nevertheless, have to do another consideration too. To apply the least square method we have to apply the logarithm to (103), but our original correlation function exhibits some negative value, so we have to scale all the values of a factor, we call 'scal', so that our formula becomes:

$$f(x) + abs(scal) = a \cdot e^{-bx} \qquad\qquad (104)$$

This consideration drives us to say that 'a' must be so that in the origin for x=0

$$a = f(0) + abs(scal) = 1 + abs(scal) \qquad (105)$$

Appling the least square method to be, taking into account this fixed value of a gives:

a= 2.88981793

b= 0.00776284 $\qquad$ (106)

Plotting the correlation function so reconstructed together with our original curve as in Figure 20, we see that the fitting one cuts the original so it makes we hope that it's possible exploiting the fitting curve determined before to obtain values of correlation for delay times smaller than 35 days. The result is observable in Figure 21.
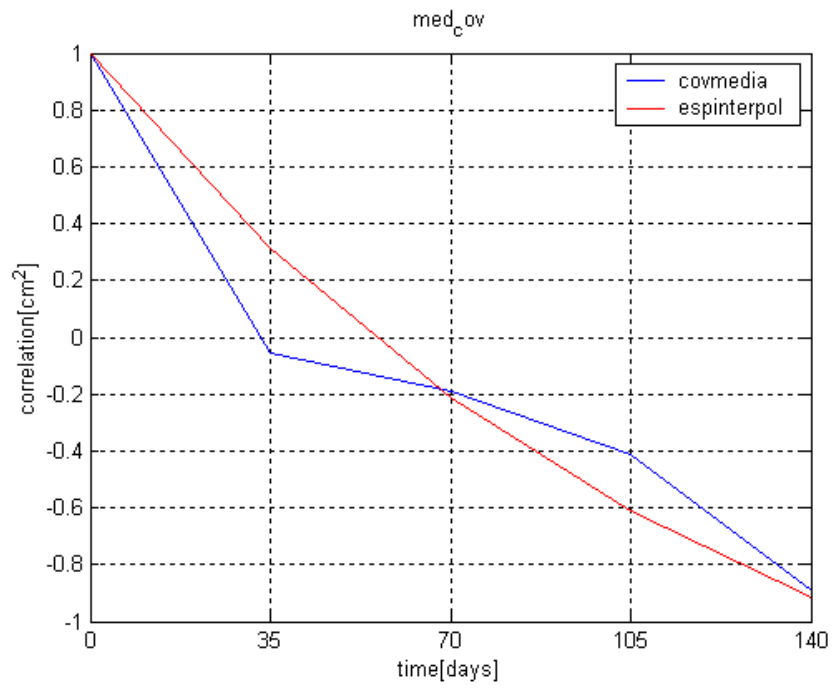
Figure 20 - Covariance computed an reconstructed
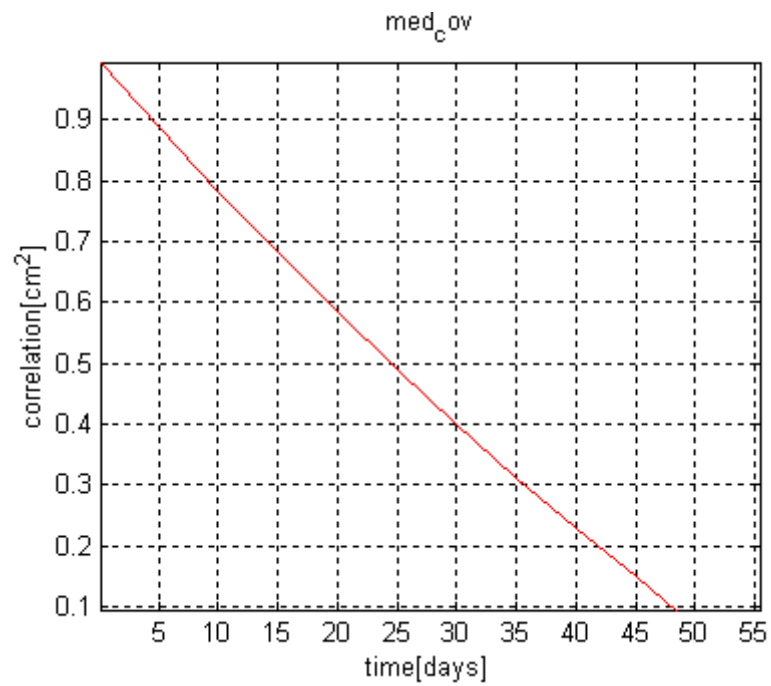
Figure 21 - Fitting curve valuated for delay times smaller than 35 days

The most interesting thing in Figure 21 is that the curve so reconstructed shows a decay of $\dfrac{1}{e}$ after a time of nearly 30 days which is exactly the result obtained by Stammer after its work of 3 years.

We, therefore, can be very satisfied of our result, because even though trough a very simple processing we obtained an analytical expression for the correlation function which is very precise.

With this result we are now ready to calculate the variance of the probability density of the noise which we must utilize to derive the conditional probability $P(\Delta h / \underline{a})$ from which it is possible to construct the maximum likelihood estimator as we'll see in the next section.

5. Maximum likelihood estimation

Recalling the formula:

$$\Delta h_{II} = C_A \delta \alpha_A + C_A S_A \delta \dot{\alpha}_A - C_D \delta \alpha_D - C_D S_D \delta \dot{\alpha}_D + N_{II} \qquad (107)$$

it is evident that we can rewrite it:

$$N_{II} = \Delta h_{II} - C_A \delta \alpha_A - C_A S_A \delta \dot{\alpha}_A + C_D \delta \alpha_D + C_D S_D \delta \dot{\alpha}_D = R \qquad (108)$$

$$P(\Delta h \backslash \underline{a}) = P(N_{II}) \qquad (109)$$

As we have seen N_{II} presents a Gaussian probability density. We can imagine that every observation related to every pixel in which we can divide the cross over regions are independent, so the global probability is only the product of the probability of every observation:

$$P(\Delta h \backslash \underline{a}) = k \exp\{-\sum_{i=0}^{n-1} \sum_{j=0}^{m-1} \frac{R^2}{2\sigma_T}\} \qquad (110)$$

We have to resolve the equations system (111) to obtain the maximum likelihood

estimator, the maximum likelihood estimate is that value of A for which the likelihood function (or equivalently the log likelihood function as in (111)) is a maximum.

$$\frac{\partial \ln[P(\Delta h \setminus \underline{a})]}{\partial \underline{a}} = 0 \qquad\qquad (111)$$

We are not interested at the moment to know how this estimator is, we are more interested, instead, to understand which is its variance. We can valuate it through the Fisher Matrix J.

Every element of this matrix is:

$$J_{ij} = -E[\frac{\partial^2 P(\Delta h \setminus \underline{a})}{\partial a_i \partial a_j}] \qquad\qquad (112)$$

The expression of J, after an opportune change of variable which rotate the two references (ascending and descending) so that their axes are parallel to the rhombs sides (but for simplicity of notation we continue to call the new variables as the old ones, meaning that behind the name of every variable there is a more or less complex function of the new variables, which are, on the contrary, easily expressible in terms of pixels indexes) is:

$$J = \frac{1}{\sigma_T^2} \begin{vmatrix} M\sum_{i=0}^{N-1} C_a^2 & -M\sum_{i=0}^{N-1} C_a C_d & \sum_{i=0}^{N-1} C_a^2 \cdot \sum_{j=0}^{M-1} S_a & -M\sum_{i=0}^{N-1} C_a C_d \cdot \sum_{j=0}^{M-1} S_d \\ -M\sum_{i=0}^{N-1} C_a C_d & M\sum_{i=0}^{N-1} C_d^2 & -\sum_{i=0}^{N-1} C_a C_d \cdot \sum_{j=0}^{M-1} S_a & \sum_{i=0}^{N-1} C_d^2 \cdot \sum_{j=0}^{M-1} S_d \\ \sum_{i=0}^{N-1} C_a^2 \cdot \sum_{j=0}^{M-1} S_a & -\sum_{i=0}^{N-1} C_a C_d \cdot \sum_{j=0}^{M-1} S_a & \sum_{i=0}^{N-1} C_a^2 \cdot \sum_{j=0}^{M-1} S_a^2 & -\sum_{i=0}^{N-1} C_a C_d \cdot \sum_{j=0}^{M-1} S_a S_d \\ -M\sum_{i=0}^{N-1} C_a C_d \cdot \sum_{j=0}^{M-1} S_d & \sum_{i=0}^{N-1} C_d^2 \cdot \sum_{j=0}^{M-1} S_d & -\sum_{i=0}^{N-1} C_a C_d \cdot \sum_{j=0}^{M-1} S_a S_d & \sum_{i=0}^{N-1} C_d^2 \cdot \sum_{j=0}^{M-1} S_d^2 \end{vmatrix}$$

$$(113)$$

Before proceeding further we must make some considerations about the geometry of the cross over regions. In our case the orbit inclination is about 97 deg, so, as we can see in Figure 22 the two orbits are nearly coincident.

In a first approximation we can consider as overlapping region the rectangular in grey depicted in the figure9 and considering they are not very rotated we can imagine as if they were perfectly coincident (rotated of 180 deg). In this case simple case the Fisher Matrix is singular, as it is obvious, because there are no elements which can introduce a difference in the accuracy with which we can know the four parameters. In a such mirror-like situation for the two orbits is sufficient knowing the accuracy of only two of the four parameter (α_A and $\dot{\alpha}_A$), because the other two are identical.

In this simple case J becomes:

$$
J = \frac{\sum\limits_{i=0}^{N-1} C_A{}^2}{\sigma_T}
\begin{bmatrix}
M & \sum\limits_{j=o}^{M-1} S_a \\
\sum\limits_{j=o}^{M-1} S_a & -M
\end{bmatrix}
\qquad (114)
$$
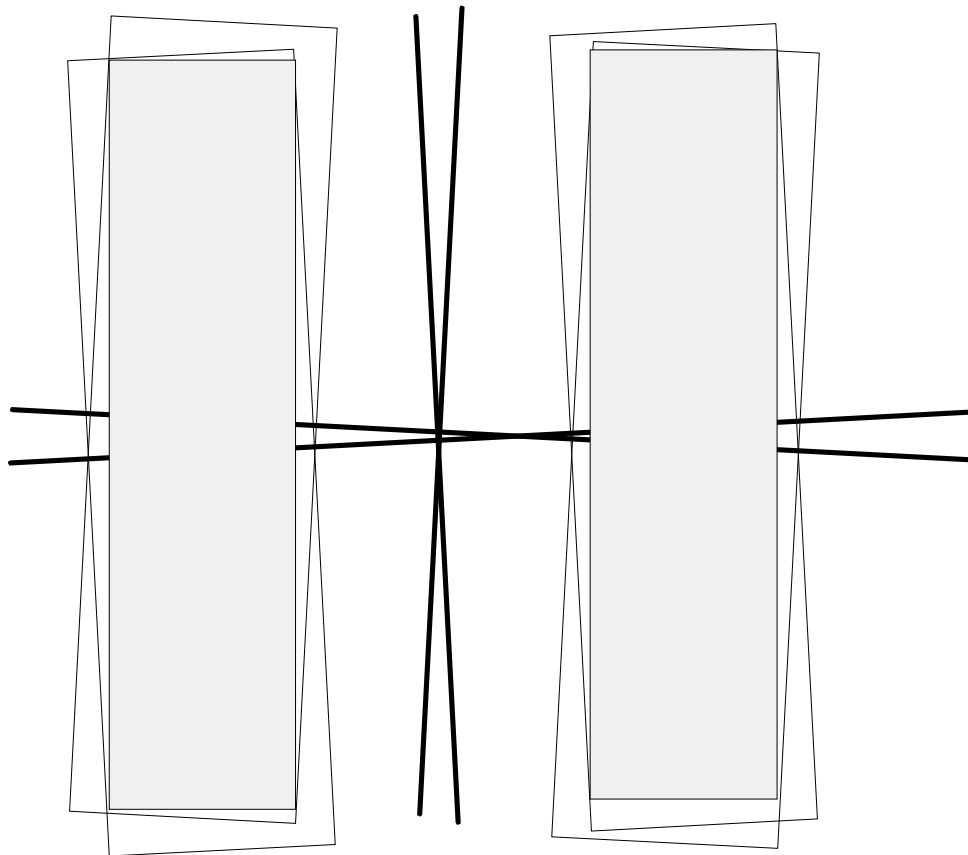
Figure 22 – Geometry of the cross-over calibration

Considering that the small inclination of the two orbits makes us loose just a pixel across track we obtained that the rectangular with which we approximate the cross over region is composed along track by 20 pixel.

Concluding, calculations were made assuming :

N=7

M=20

and considering that the cross over region are two and perfectly equal, it is possible imagine to have only a cross-over region with doble pixels either along or across track.

 The results are summarized in .Figure 23, Figure 24 and Figure 25

In .Figure 23 it's represented the uncertainty of the initial roll, in Figure 24 that of the roll derivative. The most interesting is the Figure 25, which represents their united effect , following formula (97) for the worst case, the most far pint along the cross-over regions. As we can see, for a correlation time of 5 days it respects perfectly requirements we hade
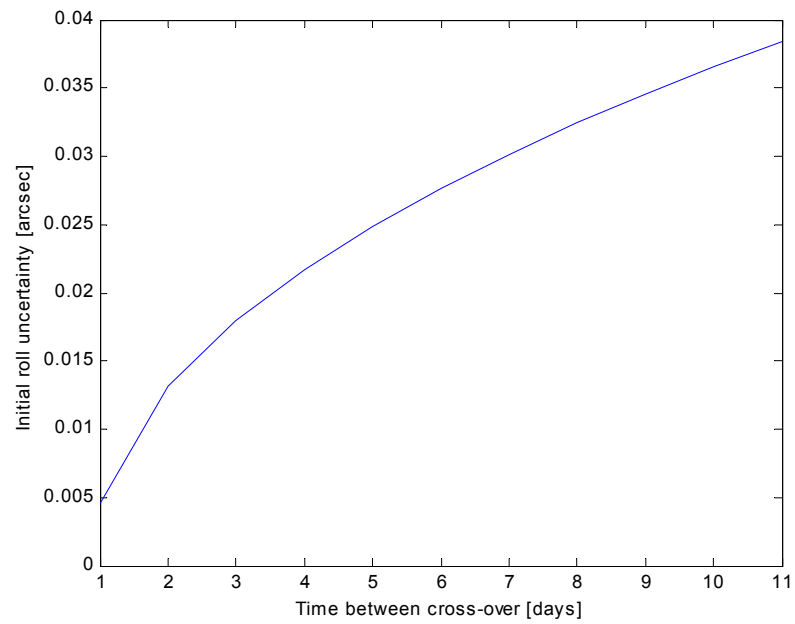
Figure 23 – Initial roll uncertainty as a function of time between cross-overs
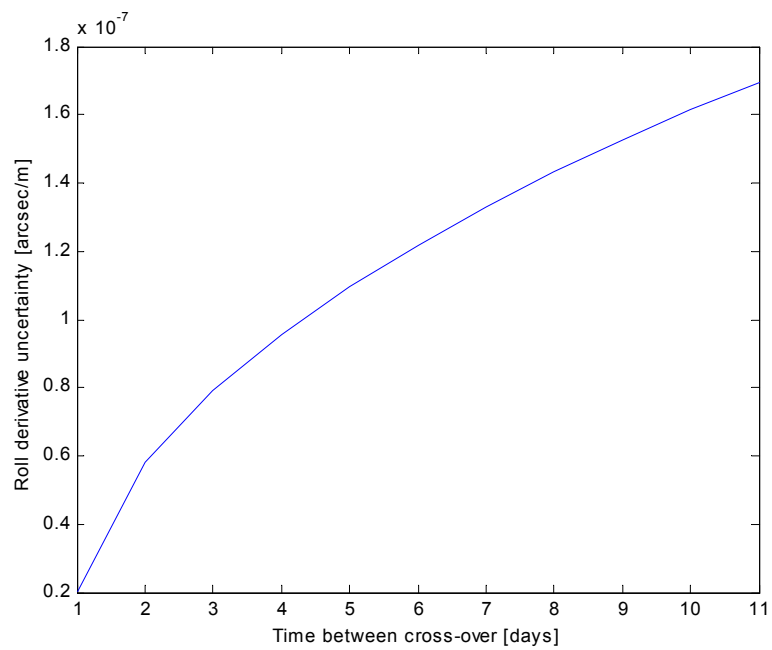
Figure 24 –Roll derivative uncertainty as a function of time between cross-overs
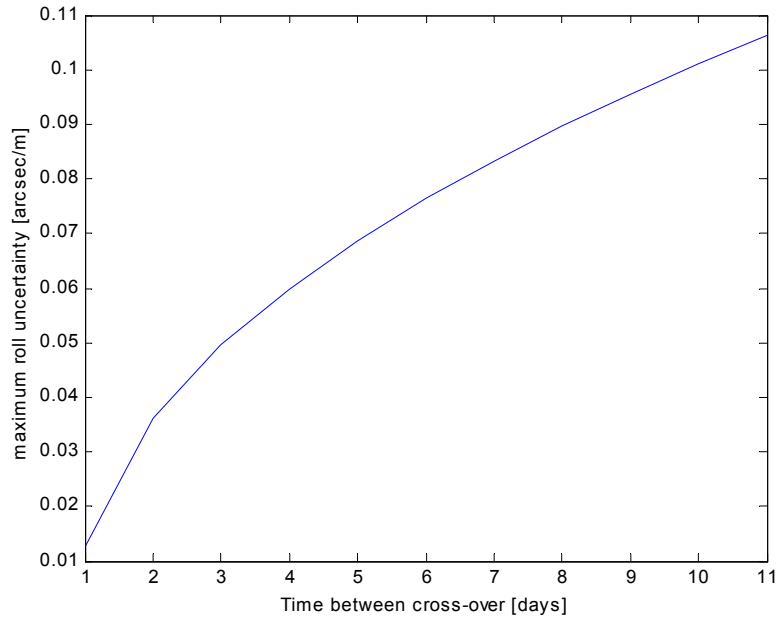
Figure 25 – Maximum roll uncertainty as a function of time between cross-overs

REFERENCES

[1] Douglas, B.C., D.C. McAdoo, and R.E. Cheney, **Oceanographic and geophysical applications of satellite altimetry**, Rev. Geophys., 25, 875--880, 1987.

[2] Wunsch, C., and E.M. Goposchkin, **On using satellite altimetry to determine the general circulation of the ocean with application to geoid improvements**, Rev. Geophys., 18, 725-745, 1980

[3] Stammer D., 1997: **Steric and wind-induced changes in TOPEX/POSEIDON large-scale sea surface topography**, J. Geophys. Res., 102, C9, 20987-21011.

[4] Vivier F., K.A. Kelly and L. Thompson, 1999: **Contributions of wind forcing, waves, and surface heating to sea surface height observations in the Pacific Ocean**, J. Geophys. Res., 104, C9, 20767-20788.

[5] Wang L. and C. Koblinsky, 1997: **Can the Topex/Poseidon altimetry data be used to estimate air-sea heat flux in the North Atlantic?**, Geophys., Res. Lett., 24, NO.2, 139-142.

[6] Behringer, D.W., **Sea surface height variations in the Atlantic Ocean: A comparison of TOPEX altimeter data with results from an ocean data assimilation system**, J. Geophys. Res., 99, 24685--24690, 1994.

[7] Bhaskaran, S., G. S. E. Lagerloef, G. H. Born, W. J. Emery, R. R. Leben, **Variability in the gulf of Alaska from Geosat altimetry data**, J. Geophys. Res., 89(C9), 16330-16345, 1993.

[8] Blaha, J. and B. Lunde, **Calibrating Altimetry to Geopotential Anomaly and Isotherm Depths in the Western North Atlantic**, J. Geophys. Res., 97(C5), 7465--7478, 1992.

[9] Chambers D.P., B.D. Tapley and R.H. Stewart, 1997: **Long-period ocean heat storage rates and basin-scale heat fluxes from TOPEX**, J. Geophys. Res., 102, C12, 163-177.

[10] Cipollini P., D. Cromwell, P. G. Challenor and S Raffaglio, **Rossby waves detected in global ocean colour data**, Geophysical Research Letters, Vol. 28 , No. 2, pp. 323-326, 2001.

[11] Cipollini P., D. Cromwell, G. D. Quartly, **Observations of Rossby wave propagation in the Northeast Atlantic with TOPEX/POSEIDON altimetry**, Advances in Space Research, Vol. 22, No. 11, pp. 1553-1556, 1999.

[12] Cipollini P., D. Cromwell, M. S. Jones, G. D. Quartly, P. G. Challenor, **Concurrent altimeter and infrared observations of Rossby wave propagation near 34° N in the Northeast Atlantic**, Geophysical Research Letters, Vol. 24, No. 8 , pp. 889-892, 1997.

[13] Kelly, K.A., M.J. Caruso and J.A. Austin, **Wind-forced variations in sea surface height in the Northeast Pacific Ocean**, J. Phys. Oceanogr., 23, 2392--2411, 1993.

[14] Nerem, R.S., B.D. Tapley and C.-K. Shum, **Determination of the Ocean Circulation using Geosat Altimetry**, J. Geophys. Res., 95(C3), 3163--3180,

1990.

[15] Challenor, P. G. and R. T. Tokmakian, 1999: **Altimeter measurements of the volume transport through the Drake Passage**. Advances in Space Research, 22(11), 1549-1552.

[16] Gaspar, P. and C. Wunsch, **Estimates from Altimeter Data of Barotropic Rossby Waves in the rthwestern Atlantic Ocean**, J. Phys. Oceanogr,. 19(12), 1821--1844, 1989.

[17] Koblinsky, C.J., R.S. Nerem, R.G. Williamson and S.M. Klosko, **Global scale variations in sea surface topography determined from satellite altimetry, in Sea Level Changes: Determination and Effects**, Geophysical Monograph Vol. 69, IUGG Vol. 11, pp. 155--165, American Geophysical Union, Washington, D.C., 1992.

[18] Le Traon, P. Y. and P. Gauzelin, 1997: **Response of the Mediterranean mean sea level to atmospheric pressure forcing,** J. Geophys. Res., 973-983.

[19] Leuliette E.W. and J.M. Wahr, 1999: **Coupled pattern analysis of sea surface temperature and TOPEX/POSEIDON sea surface height**, J. Phys. Ocean., 29, 599-611.

[20] Tapley, B.D., D.P. Chambers, C.K. Shum, R.J. Eanes, J.C. Ries, and R.H. Stewart, **Accuracy assessment of the large-scale dynamic topography from TOPEX/POSEIDON altimetry**, J. Geophys. Res., 99, 24605--24617, 1994.

[21] Tokmakian R. T. and P. G. Challenor, **Observations in the Canary Basin and the Azores Frontal Region Using Geosat Data**, Journal of Geophysical Research-Oceans, 98(C3), 4761-4773, 1993.

[22] Aoki S., Imawaki S., Ichikawa K., 1995. **Baroclinic disturbances propagating westward in the Kuroshio Extension region as seen by a satellite altimeter and radiometers**. J. Geophys. Res., 100, 839-855.

[23] Buongiorno Nardelli B., R. Santoleri, S. Marullo, D. Iudicone and S. Zoffoli, 1999: **Altimetric signal and three dimensional structure of the sea in the channel of Sicily**, J. Geophys. Res., 104, C9, 20585-20603.

[24] Fu, L.-L., **Recent progress in the application of satellite altimetry to observing the mesoscale variability and general circulation of the oceans**, Rev. Geophys. Space Phys., 21, 1657--1666, 1983.

[25] Iudicone, D., S. Marullo, R. Santoleri, and P. Gerosa, 1998: **Sea level variability and surface eddy statistics in the Mediterranean sea from TOPEX/POSEIDON data**, J. Geophys. Res., 103, 2995-3012.

[26] Joyce, T.M., K.A. Kelly, D.M. Schubert and M.J. Caruso, **Shipboard and Altimetric Studies of Rapid gulf Stream Variability Between Cape Cod and Bermuda**, Deep-Sea Res., 37, 897--910, 1990.

[27] Larnicol, G., P.Y. Le Traon, N. Ayoub and P. De Mey, 1995: **Mean sea level and surface circulation variability of the Mediterranean Sea from 2 years of TOPEX/POSEIDON altimetry**, J. Geophys. Res., 100, C12, 163-177.

[28] Larnicol, G., N. Ayoub and P.Y. Le Traon, 2001:**Majors changes in the Mediterranean Sea level variability from seven years of Topex/Poseïdon and Ers-1/2 data**, submitted to Jour Mar. Sys.

[29] Matthews, P.E., M.A. Johnson and J.J. O'Brien, **Observations of Mesoscale**

Ocean Features in the Northeast Pacific using Geosat Radar Altimetry, J. Geophys. Res., 97(C11), 17829--17840, 1992.

[30] Morrow, R., R. Coleman, J. Church, and D. Chelton, **Surface eddy momentum flux and velocity variances in the Southern Ocean from Geosat altimetry**, J. Phys. Oceanogr., 24, 10, 2050-2071, 1994.

[31] Wilkin, J., and R. A. Morrow, **Eddy kinetic energy and momentum flux in the Southern Ocean: Comparison of a global eddy-resolving model with altimeter, drifter and current-meter data**, J. Geophys. Res., 99(C4), 7903-7916, 1994.

[32] Arnault, S. and R.E. Cheney, **Tropical Atlantic sea level variability from Geosat (1985--1989)**, J. Geophys. Res., 99, 18207--18223, 1994.

[33] Arnault, S., Y. Menard and J. Merle, **Observing the Tropical Atlantic Ocean in 1986--1987 from Altimetry**, J. Geophys. Res., 95(C10), 17921--17945, 1990.

[34] Carton, J.A., **Estimates of Sea Level in the Tropical Atlantic Ocean Using Geosat Altimetry**, J. Geophys. Res., 94(C6), 8029--8039, 1989.

[35] Cheney, R.E. and L. Miller, Mapping the 1986--1987 **El Niño with Geosat Altimeter data**, EOS Trans. AGU, 69(31), 754--755, 1988.

[36] Lillibridge. J.L., R.E. Cheney and N.S. Doyle, The 1991--93 **Los Niñ–os from ERS-1 altimetry**, Proceedings Second ERS-1 Symposium, pp. 495--499, Hamburg, Germany, 1993.

[37] Egbert, G., A. Bennett and M. Foreman, **Topex/Poseidon Tides**, J. Geophys. Res., 99, 24821--24852, 1994.

[38] Andersen, O. B., and P. Knudsen: **Multi-satellite Ocean tide modelling - the K1 constituent**. In Tidal science, Eds R. Ray and P. L. Woodworth, Progress in Oceanography, Vol. 40 No 1-4, 197-216, 1997.

[39] Knudsen, P.: **Separation of Residual Ocean Tide Signals in a Collinear Analysis of Geosat Altimetry**. Bulletin Geodesique, Vol. 68, No. 1, 7-18, 1994.

[40] Knudsen, P.: **Global Low Harmonic Degree Models of the Seasonal Variability and Residual Ocean Tides from Topex/Poseidon Altimeter Data**. J. Geophys. Res. (Oceans), 99, C12, 24643-24655, 1994.

[41] Schlax, M. G. and D. B. Chelton, **Detecting aliased tidal errors in altimeter height measurements**, J. Geophys. Res., 99, 12603--12612, 1994.

[42] Bender, L.C. and Glowacki, T. 1996. **The assimilation of altimeter data into the Australian wave model**, Aust. Met. Mag., 45, 41 - 48.

[43] Francis, P.E. and Stratton, R.A. 1990. **Some experiments to investigate the assimilation of SEASAT altimeter wave height data into a global wave model**, Q. J. R. Meteorol. Soc., 116, 1225 - 1251.

[44] Freilich, M. H. and P. G. Challenor, 1994: **A New Approach For Determining Fully Empirical Altimeter Wind-Speed Model Functions**. Journal of Geophysical Research-Oceans, 99(C12), 25051-25062.

[45] Hasselmann, S., Lionello, P. and Hasselmann, K. 1997. **An optimal interpolation scheme for the assimilation of spectral wave data**, J. Geophys. Res., 102, 15823 - 15836.

[46] Janssen, P.A.E.M. 1989. **Wave-induced stress and the drag of air flow over sea waves**, J. Phys. Oceanogr., 19, 645 - 754.

[47] Janssen, P.A.E.M., Hansen, B. and Bidlot, J. 1996. **Verification of the ECMWF wave-forecasting system against buoy and altimeter data**, ECMWF Tech. Report, No. 229, ECMWF, Reading.

[48] Komen, G.J., Cavaleri, L., Donelan, M., Hasselmann, K., Hasselmann, S. and Janssen, P.A.E.M. 1994. **Dynamics and modelling of ocean waves**. Cambridge University Press, Cambridge, UK, 532 pp.

[49] Knudsen, P.: **Global high resolution mean sea surface from multi mission satellite altimetry. Physics and Chemistry of the Earth, Elsevier Science**, Berlin, in press, 1998.

[50] Born, G.H., B.D. Tapley, J.C. Ries and R.H. Stewart, **Accurate Measurement of Mean Sea Level Changes by Altimetric Satellites**, J. Geophys. Res., 91(C10), 11775--11782, 1986.

[51] Douglas, B. C., **Global sea level rise**, J. Geophys. Res., 96(C4), 6981-6992, 1991.

[52] Douglas, B. C., **Global sea level acceleration**, J. Geophys. Res., 97(C8), 12,699-12,706, 1992.

[53] Haines, B., G.H. Born and C.J. Koblinsky, **An estimate of decadal changes in sea surface topography from Seasat and Geosat altimetry, in Sea Level Changes: Determination and Effects**, Geophysical Monograph Vol. 69, IUGG Vol. 11, pp. 181--187, American Geophysical Union, Washington, D.C., 1992.

[54] Wagner, C.A. and R.E. Cheney, **Global Sea Level Change from Satellite Altimetry**, J. Geophys. Res., 97(C10), 15607--15616, 1992.

[55] Fischer J., Flemming N. C., 1999. **Operational Oceanography: Data Requirements Survey**. EuroGOOS Publication No. 12, 59 pp., ISBN 0-904175-36-7.

[56] Bosman J., Flemming N. C., Holden N. and K. Taylor, 1998. **The EuroGOOS Marine technology survey**, EuroGOOS Publication No. 4, SOC, Southampton. ISBN 0-904175-29-4.

[57] Prandle D. and N. C. Flemming, 1998. **The science base of EuroGOOS**, EuroGOOS Publication No. 6, SOC, Southampton. ISBN 0-904175-30-8

[58] Tziavos C. and N. C. Flemming 1998. **The EuroGOOS Technology Plan Working Group**, EuroGOOS Publication No. 13, SOC, Southampton, ISBN 0-904175-37-5.

[59] Pinardi N. and N. C. Flemming, 1998. **The Mediterranean Forecasting System Science Plan**, EuroGOOs Publication No. 11. SOC, Southampton, 48pp., ISBN 0-904175-35-9.

[60] Cheney, R. E., L. Miller, R. A. Agreen, N. S. Doyle, and J. L. Lillibridge, **TOPEX/Poseidon: The 2-cm solution**, J. Geophys. Res., 1994.

[61] Le Traon P.Y. and F. Ogor, 1998, **ERS-1/2 orbit improvement using TOPEX/POSEIDON: the 2 cm challenge**, J. Geophys. Res., 103, 8045-8057.

[62] Nerem, R. S., E. J. Scharma, C. J. Koblinsky, and B. D. Beckley, **A preliminary evaluation of ocean topography from TOPEX/POSEIDON mission**, J.

Geophys. Res., 99(C12), 24565-24583, 1994.

[63] Tapley, B. D., J. C. Ries, G. W. Davis, R. J. Eanes, B. E. Schutz, C. K. Shum, M. M. Watkins, J. A. Marshall, R. S. Nerem, B H. Putney, S. M. Klosko, S. B. Luthcke, D. Pavlis, R. G. Williamson, and N. P. Zelensky, **Precision orbit determination for TOPEX/POSEIDON**, J. Geophys. Res., 99(C12), 24383-24404, 1994.

[64] C. T. Allen, **Interferometric Synthetic Aperture Radar**, IEEE Geoscience and Remote Sensing Society News Letters September 1995

[65] Rodriguez, E., Martin, J. M., **Theory and Design of Interferometric Synthetic Aperture Radars, IEE Proceedings,** Vol. 139, No. 2, April 1992, pp. 147-159.

[66] **Requirements and Concepts for Topography Observing System (TOS)** – ALS Data Package February 1997- ESTEC Contract no.

[67] J.C. Curlander, R.N. McDonough, **Synthetic Aperture Radar Systems and Signal Processing**, John Wiley 1991

[68] Gary S. Brown, **"The average impulse response of a rough surface and its applications"**, IEEE Transactions on Antennas and Propagation, January 1977, pp. 67-74

[69] L. Tsang, J.A. Kong, and R.T. Shin, **Theory of Microwave Remote Sensing**, Wiley-Interscience, New York, 1985

[70] F. T. Ulaby, R. K. Moore, A. K. Fung, **Microwave remote sensing**, Volume II, Artech House, 1986

[71] Beckmann, P. and A. Spizzichino (1963), **The scattering of electromagnetic waves from rough surfaces**, Perganon Press, Oxford.

[72] M.H. Freilich and P.G. Challenor, **A new approach for determining fully empirical altimeter wind speed model functions**, J. *Geophys. Res., vol.* 99, pp. 25051-25062, 1994.

[73] D. Stammer, **Global characteristic of ocean variability estimated from regional TOPEX/Poseidon altimeter measurements**, J. Phy. Ocean., vol. 27, pp. 17433-1769, 1997

[74] C.Zelli,F,Provvedi,R.Croci **RA-2 Radar Altimeter: Instrument EM Model Performance Result**,IEEE International 1997, Vol:1.

[75] [F. Pirondini, A. Caramagno, **IRAC – Technical Note WP 3.1.3** - MISSION MODELLING, RADALT-DMS-TN-002, issue 6, 11/10/02